THESIS FOR THE DEGREE OF LICENTIATE OF ENGINEERING

# Lattice dynamics in perovskites for green energy applications

## A theoretical perspective

Petter Rosander

Department of Physics
CHALMERS UNIVERSITY OF TECHNOLOGY
Göteborg, Sweden 2022

Lattice dynamics in perovskites for green energy applications
A theoretical perspective
PETTER ROSANDER

Department of Physics
Chalmers University of Technology
SE-412 96 Göteborg, Sweden
Telephone +46 (0)31 772 10 00

Cover: Shows the future of green energy production and a boat riding on a potential energy surface.

Figures have been created using matplotlib [1], OVIOTO [2], and inkscape [3]

Chalmers digitaltryck
Göteborg, Sweden 2022

# Lattice dynamics in perovskites for green energy applications
A theoretical perspective

PETTER ROSANDER
*Department of Physics*
Chalmers University of Technology

## Abstract

Electrolyzers and fuel cells are used in green energy applications, electrolyzers split water to produce hydrogen, which can then be used in fuel cells to produce energy. Oxide perovskites have shown favorable properties for applications in this area, e.g., as electrolyte and cathode material in fuel cells and electrolyzers. The important property is the conductivity of protons, which depends sensitively on the hydrogen concentration and mobility. The concentration depends on the efficiency of the hydration reaction, which is the primary way to incorporate protons in perovskites. An example of an excellent proton conductor is acceptor doped $BaZrO_3$. Hence, some of the most crucial material properties derive from defect properties. This thesis also explore the halide perovskites $CsPbBr_3$, which have proven to be auspicious for photovoltaics. Insights into phase stability, phase transitions and the underlying dynamics in these materials are crucial. Thus, the understanding of microscopic properties is the cornerstone of this thesis.

In the present thesis, density functional theory is utilized to obtain training data for construction of potentials. The potentials that have been used are either force constant potentials or neural network potentials. The potential are then used to run lattice dynamics. To vastly extend the total simulation time or simply decrease the computational time, graphical processing units are also employed. Furthermore, defect models are applied to understand reaction kinetics.

More specifically, the vibrational defect thermodynamics of $BaZrO_3$ was examined within the harmonic approximation. We also elaborate on the soft antiferrodistortive phonon mode found in this material using self-consistent phonons and molecular dynamics. This soft mode, should ultimately be the deciding factor for which structure $BaZrO_3$ exhibit at low temperatures. Similar methods were also employed to investigate phonon dynamics in the very anharmonic perovskite, $CsPbBr_3$. These type of insights can, e.g., further guide the development of new materials by fine-tuning of properties.

**Keywords:** oxides, perovskites, defects, lattice dynamics, force constants, density functional theory, thermodynamic modelling

## LIST OF APPENDED PAPERS

I **Elaborating on the vibrational impact of defects on the hydration thermodynamics in $BaZrO_3$**
Petter Rosander and Göran Wahnström
(In manuscript)

II **Anharmonicity of the antiferrodistortive soft mode in barium zirconate $BaZrO_3$**
Petter Rosander, Erik Fransson, Cosme Milesi-Brault, Mael Guennou and Göran Wahnström
(In manuscript)

III **Transitioning from underdamped to overdamped dynamics in $CsPbBr_3$:**
**Probing the limits of the phonon quasi-particle picture**
Erik Fransson, Petter Rosander, Fredrik Eriksson, Magnus Rahm, Terumasa Tadano and Paul Erhart
(In manuscript)

The author's contribution to the papers:

I I performed all the DFT and phonon calculations and wrote the first draft of the manuscript.

II I performed all the DFT calculations. The modelling and analysis were done together with Erik Fransson. The writing of the manuscript was a joint effort.

III I performed DFT calculations and did the stochastic self-consistent harmonic approximation (SSCHA) and the self-consistent phonon (SCP) with HIPHIVE calculations.

# Contents

# List of abbreviations

**AFD** antiferrodistortive. 5, 38, 39, 42, 51

**AIMD** ab-initio molecular dynamics. 33, 37, 40

**ARDR** automatic relevance determination regression. 46, 48

**BCO** $BaCeO_3$. 5, 36

**BFO** $BaFeO_3$. 6, 7

**BZO** $BaZrO_3$. 2, 5, 6, 11, 13, 30–32, 38, 39, 41, 42, 49, 51

**CE** cluster expansion. 1, 52

**DFT** Density functional theory. 1, 2, 22, 24–27, 40, 51

**DOF** degrees of freedom. 1, 10–12, 38

**DoS** density of states. 29, 33

**EAM** embedded atom method. 40

**EHM** effective harmonic model. 37–39, 42

**FC** force constants. 27, 28, 33, 36, 38, 42, 46, 47

**FCP** force constant potential. 1, 51

**GGA** Generalized gradient approximation. 23–25

**JT** Jahn-Teller. 7, 8

**LASSO** least absolute shrinkage and selection operator. 46, 47

**LDA** Local Density Approximation. 22–25

**MD** molecular dynamics. 33, 37, 40–43, 49–51

**ML** machine learning. 46

**MSD** mean-squared displacement. 32, 42

**OLS** ordinary least squares. 45, 47, 48

**PAW** projector augmented wave. 26

**PCFC** protonic ceramic fuel cell. 15–17

**PES** potential energy surface. 7, 35

**RFE** recursive feature elimination. 46

**RMSE** root mean squared error. 45, 46, 50

**SCPH** self consistent phonon. 37–39, 42, 43, 51

**SOFC** solid oxide fuel cell. 15, 16

**SVR** support vector regression. 46, 47

**TDEP** temperature-dependent effective potential. 37–39, 42

**XC** exchange correlation. 21–24

# 1

# Introduction

In the past years, the performance of computers has increased immensely. Moreover, the ability to work collaboratively on software packages, has improved considerably with the increased connectivity. This has led to fewer, but faster and more advanced computer codes. Owing to this, the material science community has been able to run previously prohibitively expensive atomic scale simulations, for large systems and long time scales. This has furthered the possibility to use computers to search for, and optimize, material properties in all sorts of applications. These computer simulations have also made it possible to give deeper insights into experimental observations.

The solution of the Schrödinger equation, which describes the dynamics of systems on the atomic scale, scales extremely poorly with system size. The scaling problem can, e.g., be solved with Density functional theory (DFT), which have made it possible to use computers to solve the Schrödinger equation for larger systems but the smallest. However, in reformulating the Schrödinger equation, we have to pay a price, the electron-electron interaction introduces difficulties that can only be solved approximately. Despite this shortcoming, DFT has proven to be invaluable to materials science and has accelerated the search for optimal materials. For example, DFT allows for calculation of many properties on the atomic scale, such as total energies and atomic forces. Calculating the forces and energies allows for structure relaxation, i.e., low energy structures can be found, and e.g., reaction energies can be calculated using the total energy. However, despite the increased computational power, and the finesse of DFT, some simulations can still be prohibitively expensive when many degrees of freedom (DOF)s need to be considered. There are ways around this issue, one possibility is to use surrogate models that are trained with input from DFT. Such models can, e.g., be cluster expansion (CE)s, neural network potentials or force constant potential (FCP)s. These methods can then be used to examine the configurational and vibrational DOFs. We have used these types of methods to study the lattice dynamics in the proton conducting perovskite, $BaZrO_3$ (BZO), and the solar cell material, $CsPbBr_3$.

This thesis will provide an introduction to examples of proton conductive materials, more precisely the perovskite structure. Then a basic introduction to thermodynamics of points defects will be given. Following this will be a brief overview of how fuel cells and electrolyzers work. Lastly, the computational methods used to study these materials are outlined. This includes the basics of DFT and a discussion on how the electron-electron interaction is treated on different levels of DFT. Following this will be an introduction to how the nuclei system is treated and how the anharmonicity impacts the system and how it can be dealt with. Lastly, different regression and regularization methods are introduced.

# 2

# The perovskite structure

The Prussian mineralogist Gustav Rose discovered a mineral [4] which was given the name Perovskite, after the Russian mineralogist Count Lev Perovskiy. The discovery was originally of calcium titanate ($CaTiO_3$), however, many more materials exhibit the same structure, which now is known as the perovskite structure. The chemical formula is $ABX_3$, where A and B often are cations and X an anion. The B cation is 6-fold coordinated with the X anion (octahedron) while the A cation is 12-fold coordinated with the X anion (cuboctahedron). Fig. 2.1 shows the 6-fold coordination of the B cation together with the box of A cations surrounding it. The common representation of the

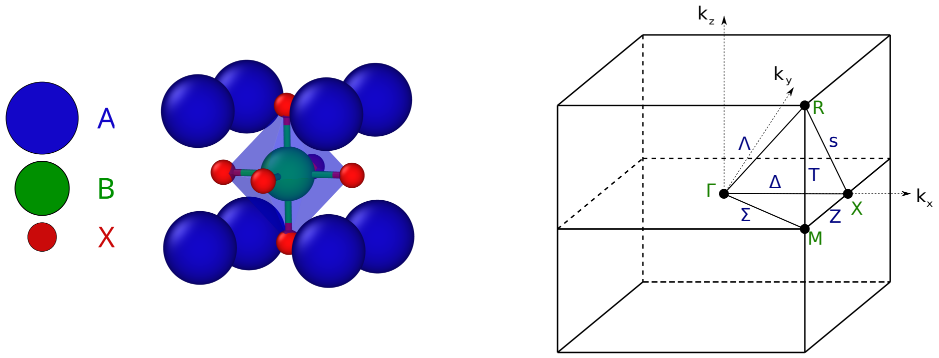

**Figure 2.1**: The ideal cubic perovskite structure together with the Brillouin zone, which shows the high symmetry points and the paths between them.

cubic perovskite is,

$$\begin{cases} A \sim (0,0,0)a_0 \\ B \sim (0.5,0.5,0.5)a_0 \\ X \sim \{(0.5,0.5,0)a_0\} \end{cases} \tag{2.1}$$

where $a_0$ is the lattice constant and $\{\}$ indicates cyclic permutation. The unit cell of the reciprocal lattice of the cubic structure, with its high symmetry points and paths between the high symmetry points, is shown in Figure 2.1.

There exist a vast number of perovskites owing to the extensive possible paring of the A and B site ions. However, the possible paring of the A and B ions for ionic perovskites is restricted by the charge neutrality condition, which is that the oxidation numbers must sum to zero. For an oxygen perovskite, we have three possible parings of oxidation state for the A and B ions, namely, 1:5, 2:4 and 3:3. Substitutional defects on the A and B sites give a large pool of possible materials, one such class of materials is the high-entropy perovskite oxides [5, 6]. Another class of trending materials is the hybrid perovskites, where the X atom is occupied by a halide anion, e.g., Br. The A site can be occupied by e.g., Cs, but also molecules such as formamidinium and lastly, the B site is a bivalent metal cation such as Pb. These class of materials are relevant in, e.g., solar cells, photodetectors or nanolasers [7–10].

Thanks to the vast number of materials, the perovskite structure has shown numerous of novel properties, such as, triple conduction of electrons, protons, and oxygens [11], proton conductivity [12], piezoelectricity [13], multiferroicity [14], dielectricity [15] and magnetocalorimetry [16].

## 2.1 Phases of the perovskite structure

Few perovskites exhibit the ideal cubic structure, most unit cells are instead distorted to e.g., orthorhombic, tetragonal or trigonal cells. Goldschmidt derived an empirical formula for determining if the perovskite would exhibit the cubic structure or not, which is referred to as the Goldschmidt tolerance factor [17]. Assuming that the perovskites are mostly ionic, we can model the ions as hard spheres. We can then derive the ratio of how well different ionic radii [18] match along different axis of the crystal. Measuring the lattice constant along the B-X axis gives a lattice constant of $a = 2(R_B + R_X)$, whereas measuring along the A-X axis gives $a = \sqrt{2}(R_A + R_X)$. The tolerance factor is then given as the fraction of the lattice constants along different crystal axis,

$$t = \frac{R_A + R_X}{\sqrt{2}(R_B + R_X)}.$$

The closer the tolerance factor is to 1 the more likely it is that the structure will exhibit the ideal cubic structure. However, it is important to remember that it should serve as

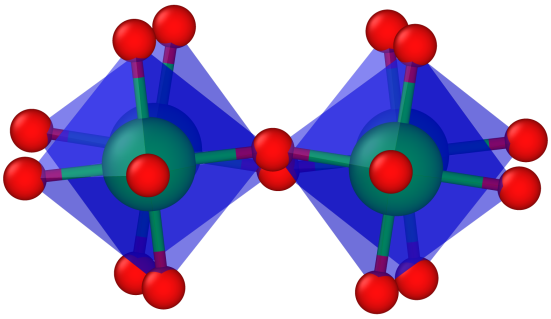

**Figure 2.2:** A schematic representation of the tilting of the oxygen octahedra. The distortion is exaggerated for visualization purposes.

a guide rather than a rule.

Perovskites with a tolerance factor larger than 1 are usually distorted to a tetragonal or hexagonal lattice, the B ion is too small, and the lattice will develop polar distortions, such as in $BaTiO_3$ [19]. On the other hand, a smaller tolerance factor indicates that the A ion is too small and can't effectively bind with all neighboring oxygen ions. The structure commonly distorts to an orthorhombic cell, e.g., $CaTiO_3$, $CdTiO_3$ [20] and $BaCeO_3$ (BCO) [21].

## 2.2 Barium Zirconate

A good candidate to preserve the cubic symmetry all the way down to 0 K is $BaZrO_3$ BZO, as the tolerance factor is close to 1 ($\sim 1.01$). However, depending on the approximation used in the first principle calculations, a symmetry lowering phase appears as an imaginary frequency at the R-point of the reciprocal lattice. The competing structure for BZO is the antiferrodistortive (AFD) structure, where the oxygen octahedra $[ZrO_6]$ is rotated. Successive cells are rotated in opposite direction (out of phase). Fig. 2.2 depicts the distortion. This distortion has been shown to be strongly related to the Goldschmidt tolerance factor [22]. However, it is still debated whether BZO is cubic all the way down to 0 K [23–31].

Experimental sintering of BZO is difficult because of its high melting temperature and long soaking times [32]. BZO is therefore commonly studied using powder samples [23, 26, 33]. For example, Akbarzadeh *et al.* [23] studied BZO using x-ray and neutron diffraction on a powder sample together with Monte Carlo simulations using an effective Hamiltonian. They found that the structure remained cubic all the way down to at least 2 K. Moreover, Perrichon *et al.* [26] found that the cubic phase can be ascribed down to at least 3 K using neutron powder diffraction. They measured the dynamical structure factor at the R-point at different temperatures and revealed a weak frequency dependence with temperature, which agreed well with the theoretical calculation. Furthermore, they studied the stability of the cubic structure with first principles calculations and found that the predicted ground state depended on the approximation used, which can also be noted from several other first principles studies [27–30]. They also found that the instability correlates strongly with the lattice spacing, and the cubic structure is stabilized by a large cell size. Yang *et al.* studied BZO at room temperature and high pressure, they found that BZO undergoes a phase transition from cubic to tetragonal under high pressure which corroborates the correlation of the lattice parameter and stability of the cubic structure. Furthermore, Toulouse *et al.* [31] investigated the Raman spectrum. This spectrum should be completely silent for the cubic perovskite, however, in this case it exhibited peaks. They attributed a majority of the contributions to the Raman spectrum to overtones. In principle, the Raman spectrum should probe the $\Gamma$ point, however overtones can still obey the selection rules in two phonons process where the momentum of the two phonons has opposite sign but equal amplitude. They conclude that locally tilted nanodomains are not supported by the Raman spectrum.

On the other hand, Giannici *et al.* [24] conducted x-ray diffraction and Raman spectroscopy on BZO and Y doped BZO, they found that the undoped sample's x-ray diffraction pattern was consistent with a cubic perovskite. However, the Raman spectrum exhibited peaks. They assigned these peaks to local symmetry reduction due to local tilting of the oxygen octahedra. Similarly, Levin *et al.* [25] observed evidence for a local symmetry reduction as well. They studied BZO using transmission electron microscope and observed a weak but yet discrete spot around the R-point ($^1/_2 hkl$). The spot appeared below 80 K and therefore suggests that there exist nanodomains of octahedral rotated cells below this temperature.

## 2.3 Barium Ferrite

The ground state structure of $BaFeO_3$ (BFO) is not extensively studied experimentally. However, there exist some experimental studies on the manufacturing of BFO both in bulk and as epitaxial thin films. The bulk manufacturing found numerous of phases depending on the conditions during the fabrication, e.g., ambient, heating temperature and duration of heating is important [34, 35]. Hayashi [36] synthesized the cubic structure of BFO by low temperature oxidation of $BaFeO_{2.5}$ and found from neutron diffraction that it remained cubic down to at least 8 K. Alternatively, the cubic structure can be stabilized by doping with, e.g., Ce on the Ba site [37]. Epitaxial BFO thin films grown on $BaTiO_3$ exhibited a pseudo cubic structure that was nonconductive and weakly ferromagnetic. However, this nonconductivity and weakly ferromagnetism seem to be

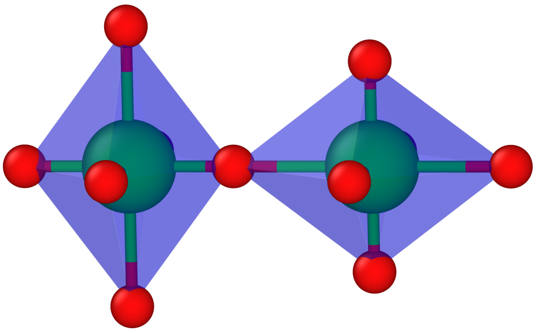

**Figure 2.3:** A schematic representation of the Jahn-Teller mode. The distortion is exaggerated for visualization purposes.

related to the oxygen content, and therefore the valency of the iron. After annealing in oxygen, the films became conductive and ferromagnetic [38]. Matsui *et al.* found similar results [39].

Computationally, Rahman *et al.* [40] found that BFO has a ferromagnetic ground state structure for all approximations they tested. They also found that strained structures can transform from ferromagnetic to ferrimagnetic and with even larger strains to anti-ferromagnetic. Cherair *et al.* [41] did an exhaustive first principle study of BFO where they investigated the potential energy surface (PES) for a few modes using different approximations. They found that the Jahn-Teller (JT) distortion minimizes the total energy, however, the difference in energy depends strongly on the value of U used in the DFT+U method (see Chapter 5). Larger U values tend to stabilize the cubic structure. Furthermore, they qualitatively concluded that the JT structure could be introduced by epitaxial strain. They also found that the exchange interaction from Hartree-Fock (see Chapter 5) tends to localize the electrons on the iron atom since the magnetic moments of the iron increases, this is inline with what larger U values produce as well. Finally, Hoedl *et al.* [42], found that the ground state structure of BFO is the JT structure, see Fig. 2.3, for DFT + U with U = 4 eV.

The JT effect is a geometrical distortion of the atoms associated with a magnetic electronic ground state. This distortion was first discussed by Hermann Jahn and Edward Teller, who used symmetry arguments to show that any nonlinear molecule with a spatially degenerate electronic ground state will be unstable and distort in such a way that the states will lift its degeneracy [43]. This type of distortion is common in solid state metal complexes, with high spin configurations such as $d^4(t_{2g}^3 e_g^1)$ occupations. In BFO the distortion is driven by the covalency of the Fe-O bond. A schematic representation of the orbital occupations is given in Figure 2.4. The $e_g$ orbitals are the ones pointing directly towards the ligands (oxygens). For this specific paring of the electrons, there

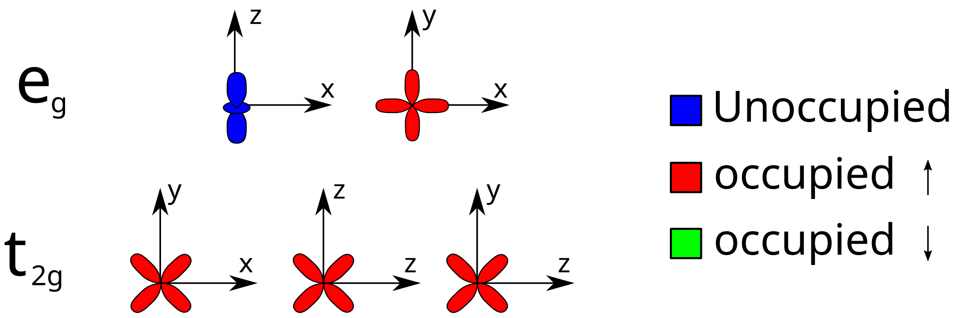

**Figure 2.4:** A schematic representation of the electron paring of the iron atom in a high spin $t_{2g}^3 e_g^1$ state. The iron atom is located in the origin and the oxygens are located along the Cartesian axes.

will be a larger concentration of electrons in the xy plane. The larger concentration of electrons within the xy plane leads to a repulsive interaction between the oxygen and iron which elongates the Fe-O bond. This elongation reduces the energy of the $d_{x^2-y^2}$ orbital and lifts the degeneracy of the orbitals. The lowering of the energy in the $d_{x^2-y^2}$ orbital is what drives the distortion. In response to this elongation the oxygen's along the z direction contracts slight, due to reduced electrostatic repulsion (elasticity). One can also imagine that the electron instead was situated in the $d_{z^2}$ which would lead to an elongation along that bond and a contraction in the xy plane using the same arguments. An excellent discussion on the JT effect can be found in Ref. [44].

# 3

# Thermodynamics of point defects

Point defects are impurities in an otherwise pristine material. Formation of defects is mostly driven by the increased entropy of the system, and can drastically change the properties of a material. Therefore, controlling the types of defects that are formed can lead to new technological advances [45].

Defects can be intrinsic, that is, the defect involves the atomic species of the host lattice. The defect can also be extrinsic, which involves atomic types that are not native to the host lattice. Examples of point defects are vacancies, self-interstitals, interstitials and substitutional defects. Kröger-Vink notation is typically used to denote these types of defects. This convention describes the effective electronic charge and lattice position of the considered defect. The notation looks as follows, $\mathrm{A}_{\mathrm{C}}^{\mathrm{B}}$, where the letter, A, denotes the defect, a vacancy will have the symbol v, for example. The B is the effective charge which can be x, $\bullet$ or $'$ for a neutral, positive, or negative effective charge, respectively. The effective charge is defined as the difference in the charge between the site when it is occupied by the defect compared to the host atom. Lastly, the C denotes the position in the host lattice, e.g., an interstitial will be denoted by an i.

An example is, $\mathrm{v}_{\mathrm{O}}^{\bullet\bullet}$, which is an oxygen vacancy that has an effective charge of +2. $\mathrm{Y}_{\mathrm{Zr}}'$ is a substitutional defect where an yttrium is situated on a zirconium site with an effective charge of -1. $\mathrm{H}_{\mathrm{i}}^{\bullet}$ is a proton interstitial, which, in this work, will typically be denoted $\mathrm{OH}_{\mathrm{O}}^{\bullet}$ since the proton is very strongly bound to the oxygen. Lastly, $\mathrm{O}_{\mathrm{O}}^{\times}$ is and oxygen situated on its regular lattice site with an effective charge of 0. The formation of point defects is governed by thermodynamics, for which the relevant equations and concepts for this thesis will be presented in this chapter.

## 3.1 Point defect formation

Gibbs free energy dictate what defects are formed, it is defined as,

$$G(T,P) = U - TS + PV,$$

where $U = \langle E \rangle$ is the internal energy, $S = -k_B \langle \ln(p) \rangle$ is the entropy, where $p$ is the probability of a state being occupied, $P$ and $V$ are the pressure and volume respectively. $\langle A \rangle$ defines an average of the observable $A$,

$$\langle A \rangle = \sum_i p_i A_i.$$

The equilibrium number of point defects is then found by calculating the change in free energy upon defect formation,

$$\Delta G(T,P) = \Delta H - T\Delta S, \tag{3.1}$$

where $H$ is the enthalpy, $H = U + PV$. Considering all DOF, configurational, electronic and vibrational in the free energy simultaneously is, however, computationally intractable. Fortunately, the relevant timescales for the DOF are considerably different. This allows us to coarse-grain the problem, i.e., the DOF can be treated independently of each other. Assuming that the difference in electronic entropy is negligible, we arrive at,

$$\Delta S = \Delta S_{\text{conf}} + \Delta S_{\text{vib}}.$$

Furthermore, if the defects are non-interacting, the Free energy difference, Eq. (3.1), simplifies to,

$$\Delta G = n\Delta G^f_{\text{def}} - T\Delta S_{\text{conf}}. \tag{3.2}$$

where $n$ is the number of defects, $\Delta G^f_{\text{def}}$ is the formation energy of an isolated defect and $\Delta S_{\text{conf}}$ is the configurational formation entropy. Moreover, since we have assumed that the defects are non-interacting, the probability of all the states should be equal, i.e., $p = \Omega^{-1}$, where $\Omega$ is the number of microstates, denoted multiplicity. This approximation leads to a simpler expression for the configurational entropy given as,

$$\Delta S_{\text{conf}} = k_B \ln \Omega. \tag{3.3}$$

The multiplicity is given by the binomial coefficient, i.e., we want to place n defects on $N$ possible sites,

$$\Omega = \binom{N}{n}. \tag{3.4}$$

This is slightly modified in the case of, e.g., interstitial defects that have an internal DOF, such as a rotation. For example, the proton in BZO ($\mathrm{OH}_\mathrm{O}^{\bullet}$), is free to rotate in a plane with $m = 4$ distinct positions [46]. This leads to an extra factor in the multiplicity,

$$\Omega = m^n \binom{N}{n}. \tag{3.5}$$

Using Stirling's approximation in Eq. (3.3), allows us to derive an equilibrium concentration. This concentration is found by minimizing Eq. (3.2) w.r.t to $n$, i.e.,

$$\frac{d}{dn}\Delta G = \Delta G^f_{\mathrm{def}} + k_B T \ln\left(\frac{n}{m(N-n)}\right) = 0. \tag{3.6}$$

This leads to the following relation,

$$x_{\mathrm{eq}} = \frac{m\exp\left(-\frac{\Delta G^f_{\mathrm{def}}}{k_B T}\right)}{m\exp\left(-\frac{\Delta G^f_{\mathrm{def}}}{k_B T}\right) + 1},$$

where $x = n/N$. In the dilute limit, ($x \ll 1$), this simplifies to,

$$x_{\mathrm{eq}} = m\exp\left(-\frac{\Delta G^f_{\mathrm{def}}}{k_B T}\right),$$

where the free energy difference, is given as,

$$\Delta G^f_{\mathrm{def}} = \Delta E_{\mathrm{el}} + \Delta F_{\mathrm{vib}} + \sum_i \Delta n_i \mu_i + q\mu_e + P\Delta V_{\mathrm{def}}. \tag{3.7}$$

Here, the electronic and vibrational energy have been separated with the same argument as for the entropy. This means that, $\Delta E_{\mathrm{el}}$ is the electronic defect formation energy, $\Delta F_{\mathrm{vib}}$ is the vibrational free energy of formation and $\Delta V_{\mathrm{def}}$ is the defect formation volume. Further, $\Delta n_i$ is the number of removed/added atomic species and $\mu_i$ is the corresponding chemical potential. Lastly, q is the effective charge of the defect and $\mu_e$ is the Fermi energy.

## 3.2 Chemical reactions

For a general reaction,

$$n_A A + n_B B \rightleftharpoons n_c C + n_D D,$$

we can derive an equilibrium concentration similarly to the defect reaction. First, note that the chemical potential describes the Gibbs free energy associated with a removal or addition of an atom from a reference state, that is,

$$\mu_i = \left(\frac{\partial G}{\partial n}\right)_{T,P},$$

which is given as (Cf. Eq. (3.6)),

$$\mu_i = \mu_i^0 + k_B T \ln(c_i).$$

Further, for an equilibrium, we know that the chemical potential of the product and reactant should be equal, i.e.,

$$n_A \mu_A + n_B \mu_B = n_c \mu_C + n_D \mu_D.$$

After some rearrangements, we find that the equilibrium concentrations will be given by,

$$\frac{c_C^{n_C} c_D^{n_D}}{c_A^{n_A} c_B^{n_B}} = \exp\left(-\frac{\Delta G^\circ}{k_B T}\right),$$

where $\Delta G^\circ = n_c \mu_c^\circ + n_D \mu_D^\circ - n_A \mu_A^\circ - n_B \mu_B^\circ$.

The hydration reaction, which has almost exclusively been studied throughout this thesis, is the dissociative filling of a vacancy by a hydroxide group and the protonation of a regular oxygen site,

$$\mathrm{H_2O} + \mathrm{O_O^X} + \mathrm{v_O^{\bullet\bullet}} \rightleftharpoons 2\,\mathrm{OH_O^{\bullet}}. \tag{3.8}$$

This leads to an equilibrium equation given by,

$$K(T) = \frac{[\mathrm{OH_O^{\bullet}}]^2}{[\mathrm{v_O^{\bullet\bullet}}][\mathrm{O_O^X}] p_{\mathrm{H_2O}}} = 4^2 \exp\left(-\frac{\Delta G^\circ}{k_B T}\right),$$

where K(T) is the equilibrium constant and [A] is the concentration of A. Here, the chemical potential of steam has been used, which is given by,

$$\mu_{\mathrm{H_2O}}(T, p_{\mathrm{H_2O}}) = \mu_{\mathrm{H_2O}}^\circ + k_B T \ln\left(\frac{p_{\mathrm{H_2O}}}{p^\circ}\right),$$

and thus, $p_{\mathrm{H_2O}}$, is the partial pressure of steam and $p^\circ$ is the reference pressure. The term $4^2$ stems from the internal rotational DOF of the proton Eq. (3.5). This term can be incorporated into $\Delta G^\circ$ by moving it into the exponential. This would then rescale the vibrational entropy as,

$$\Delta S_{\mathrm{app}} = \Delta S_{\mathrm{vib}} + 2 k_B \ln 4.$$

In experiments, the mass change under a wet condition can be recorded and, together with the site restriction, the equilibrium constant can be plotted as a function of temperature in a van't Hoff plot. The hydration enthalpy and entropy will then be given by the slope and intercept, respectively, in the van't Hoff plot. This gives us a direct comparison between experiments and theory.

Evidently, the hydration reaction, Eq. (3.8), requires oxygen vacancies to be present in the material. Due to the increased configurational entropy of the system with defects, some oxygen vacancies will natively be present. However, it is also possible to engineer the material in such a way that more oxygen vacancies will be present. In, for example BZO, this can be done by acceptor doping. One of the most promising acceptor dopant for BZO is yttrium, which is incorporated on the B site [47, 48]. Incorporation of yttrium and oxygen vacancies can, e.g., be done by the following reaction,

$$\mathrm{Y_2O_3} + 2\,\mathrm{Zr}_{\mathrm{Zr}}^{\times} + \mathrm{O}_{\mathrm{O}}^{\times} \rightleftharpoons 2\,\mathrm{Y}_{\mathrm{Zr}} + \mathrm{v}_{\mathrm{O}}^{\bullet\bullet} + 2\,\mathrm{ZrO_2},$$

as done in [49]. However, B site doping, such as yttrium doping, is associated with defect trapping, where, e.g., the proton becomes strongly bound to the oxygen close to an yttrium [12, 50]. This trapping can either inhibit or promote hydration, depending on the ration between proton and vacancy trapping [51]. This trapping can also inhibit proton mobility and may lead to lower performing devices, such as for the fuel cells, which is discussed in Chapter 4. Therefore, A site doping has also been explored by first principle calculations in [52] which suggests that A site doping could reduce the degree of proton trapping, however, experimental investigations of A site doping are scarce.

# 4

# Electrolyzers and fuel cells

Fuel cells and electrolyzer are important for the sustainability of our society. Some authors have regarded “sustainability” as a meaningless word due to its many definitions [53]. Nevertheless, if we consider that the meaning of the word is similar to that of sustainable development, it is apparent what problems this thesis aims to help solve. Sustainable development was defined in the Brundtland report, 1987 [54], “Sustainable development seeks to meet the needs and aspirations of the present without compromising the ability to meet those of the future…”. We may thus conclude that we need a new era of energy production since the burning of fossil fuels has severe impact on both the current, and future generations [55–57]. The hydrogen economy may very well be part of the solution [58, 59].

Therefore, this thesis applies the computational methods mentioned in Chapter 1 to study proton conducting electrolytes and mixed conducting cathodes. The possible applications of these materials is in, e.g., fuel cells and electrolyzers. Electrolyzers produce hydrogen and oxygen gas by splitting water using electricity, while the fuel cells run the process in reverse, producing electricity and water by consuming hydrogen and oxygen gas.

The hydrogen produced by the electrolyzer can be stored in a multitude of ways, e.g., by liquifying or pressurizing it. The advantage of storing energy in an intermediate form such as hydrogen gas is that the energy can be used much later [59]. Electrolyzers can thus be used in combination with, e.g., solar, wind or hydro energy to store the excess electricity as hydrogen when the demand is low. The hydrogen can then later be used in fuel cells to produce energy when the demand is higher.

There exist a few different types of cells, e.g., polymer electrolyte membranes (PEM), protonic ceramic fuel cell (PCFC) and solid oxide fuel cell (SOFC). However, the materials that have been studied in this thesis are used in the PCFC, but some materials can also be used in the SOFC. The PCFC conducts protons, while the SOFC conduct oxygen

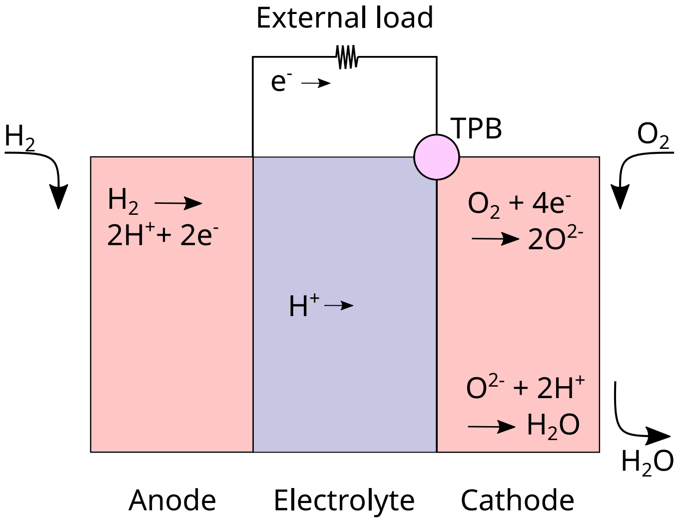

**Figure 4.1**: Operation of a protonic ceramic fuel cell

ions through the electrolyte. Furthermore, the anode and cathode side is catalytically active, meaning that, e.g., on the anode side hydrogen is able to bind to the surface and then dissociate. There are benefits, and drawbacks, with both types of cells. For example, the large migration barrier of the oxygen in the SOFCs requires high operating temperatures, (800°C-1000°C). This leads to long start up and shutdown times, but also to thermal and chemical stress, which shortens the lifespan of the device. However, the high operating temperature of the SOFC offer a greater fuel flexibility, as the reduced oxygen can form a large variety of oxides on the anode side [60]. For an overview of the SOFC see, e.g., Ref. [61]. The operating temperature for the PCFCs is 400°C-700°C which is significantly lower. Another benefit of the PCFC is that the water is formed on the cathode side, i.e., the product does not dilute the fuel. See e.g., Ref. [62, 63] for more information on the PCFC.

Fig. 4.1 shows the operation of the PCFC, the anode splits hydrogen into protons and electrons, the electron is then carried through an external load while the protons are conducted through the electrolyte. The cathode absorbs the oxygen gas on the surface and the electrons reduces the oxygen and reacts with the protons to form water. The cathode can either be a mixed conductor, conducting both protons and electrons and in some cases even oxygen as well, or simply a proton conductor. The benefits of the cathode material being a mixed conductor is that the reactive zone is extended from the triple phase boundary (TPB), which is marked in Fig. 4.1, to the whole surface of the cathode. Amezawa *et al.* [64] investigated the importance of the reactive zone experimentally. They found that the triple phase boundary was the dominant reactive site in the low temperature range. However, for higher temperatures, the double phase boundary became dominant.

Barium zirconate and cerate has proven to be a good proton conductor [65, 66], however, the sintering of the material is difficult, and the stability is an issue [67, 68]. Good performing and durable PCFCs has recently been manufactured [69, 70] using doped barium cerate. We studied the vibrational hydration entropy and enthalpy of barium zirconate in **PAPER I**.

# 5

# Electronic structure theory

The Schrödinger equation describes the dynamics of systems on the atomic scale. It gives physical insight into both the structural and chemical properties of materials. However, solving it for even the smallest system is a formidable task. The time-independent Schrödinger equation is usually written in a deceptively easy form,

$$\mathscr{H}\Psi_n(\mathbf{R},\mathbf{x}) = \mathscr{E}_n\Psi_n(\mathbf{R},\mathbf{x}).$$

where $\Psi_n(\mathbf{R},\mathbf{x})$ is the wave function, $\mathbf{R}$ encodes the nuclear positions and $\mathbf{x}$ describes the spin, $\sigma$, and position, $\mathbf{r}$, of the electrons, $\mathscr{E}_n$ is the energy of the system. The Hamiltonian $\mathscr{H}$ includes a description of all interactions that are taken into account. It is conveniently written in atomic units, where the mass and charge of the electron together with $\hbar$ and $4\pi\epsilon_0$ is set to 1. In the absence of any external fields it reads,

$$\begin{aligned}\mathscr{H} = &-\sum_i \frac{\nabla_i^2}{2} + \frac{1}{2}\sum_{i\neq j}\frac{1}{|\mathbf{r}_i - \mathbf{r}_j|} - \sum_k\sum_i \frac{Z_k}{|\mathbf{R}_k - \mathbf{r}_i|}\\ &-\sum_k \frac{\nabla_k^2}{2m_k} + \frac{1}{2}\sum_{k\neq n}\frac{Z_kZ_n}{|\mathbf{R}_k - \mathbf{R}_n|},\end{aligned}$$

where $m_k$ and $Z_k$ is the mass and charge of the kth nucleus. The first and fourth term is the kinetic energy of the electronic and nuclear system, the other terms are the Coulomb interactions, for example, the second term is the repulsion between the electrons which presents most of the difficulty. This equation is separated into two decoupled equations by assuming that the electronic system reacts instantaneously to any change in the ionic system due to the much smaller mass of the electrons. This is what is known as the Born-Oppenheimer approximation [71] and leads to the following

Hamiltonian for the electronic system,

$$\mathscr{H}_{\mathrm{el}} = -\sum_i \frac{\nabla_i^2}{2} + \frac{1}{2}\sum_{i\neq j} \frac{1}{|\mathbf{r}_i - \mathbf{r}_j|} - \sum_k \sum_i \frac{Z_k}{|\mathbf{R}_k - \mathbf{r}_i|}, \tag{5.1}$$

where the ionic position is fixed and represents an external potential. The ionic system is treated in Chapter 6. This equation is still only possible to solve for the smallest systems, since the size of the Hamiltonian grows factorially with the number of electrons [72]. Thus, further simplifications are needed.

## 5.1 The Hohenberg-Kohn theorem

Hohenberg and Kohn [73] recognized that the ground state density of the Hamiltonian in Eq. (5.1) is uniquely defined by the external potential. Therefore, they concluded that we may work with the electron density instead of the wave function, which means that the problem has been reduced to a problem of three coordinates. The corresponding energy functional is then given by,

$$\begin{aligned}\mathscr{E}_{HK} &= \langle \Psi[n(\mathbf{r})] | \mathscr{H}_{\mathrm{el}} | \Psi[n(\mathbf{r})] \rangle \\ &= T[n(\mathbf{r})] + V[n(\mathbf{r})] + \int \mathrm{d}\mathbf{r}\; n(\mathbf{r}) V_{\mathrm{ext}}(\mathbf{r}).\end{aligned} \tag{5.2}$$

The kinetic energy functional, $T[n(\mathbf{r})]$, and electron Coulomb interaction, $V[n(\mathbf{r})]$, are system independent. Therefore, in principle, they could be determined once and then be applied to all systems. However, the exact functional form is still unknown. Fortunately, the variational principle tells us that the density that minimizes the energy functional in Eq. (5.2) is the true ground state density. This minimization is constrained by the normalization of the electron density,

$$\int \mathrm{d}\mathbf{r}\; n(\mathbf{r}) = N$$

where $N$ is the total number of electrons. Hohnberg and Kohn only proved that we may work with the density to find the ground state energy. However, they provided no computational strategy on how to solve the minimization problem.

Hohnberg and Kohn were not the only ones who proposed that one could work with a density functional, previous work by, e.g., Thomas [74], Fermi [75] and Dirac [76] explored the possibility of using the electron density as a fundamental variable.

## 5.2 The Kohn-Sham formulation

Fortunately, Kohn and Sham provided an algorithmic scheme on how to solve the minimization problem. The idea behind the Kohn-Sham computational scheme [77] is that an effective potential in a non-interacting auxiliary system can be used to mimicking the interacting system. That is, they sought an effective potential, $V_{\text{eff}}(r)$, that represents the interactive system such that a single particle equation,

$$\left[-\frac{1}{2}\nabla^2 + V_{\text{eff}}(r)\right]\psi_n(r) = \varepsilon_n \psi_n(r), \tag{5.3}$$

can be solved instead. The corresponding energy functional for this non-interacting auxiliary system is then,

$$\mathscr{E}_s[n(\mathbf{r})] = T_s[n(\mathbf{r})] + \int \mathrm{d}\mathbf{r}\; V_{\text{eff}}(\mathbf{r})n(\mathbf{r}). \tag{5.4}$$

Another key insight that Kohn and Sham had was to rewrite the energy functional in Eq. (5.2) as,

$$\mathscr{E}[n(\mathbf{r})] = T_s[n(\mathbf{r})] + \frac{1}{2}\int \mathrm{d}\mathbf{r}'\; \frac{n(\mathbf{r})n(\mathbf{r}')}{|\mathbf{r}-\mathbf{r}'|} + \mathscr{E}_{xc}[n(\mathbf{r})] + \int \mathrm{d}\mathbf{r}\; V_{\text{ext}}(\mathbf{r})n(\mathbf{r}), \tag{5.5}$$

where the kinetic energy of the non-interacting system, $T_s[n(\mathbf{r})]$, and the Hartree term have been added and subtracted. The exchange correlation (XC) energy functional, $\mathscr{E}_{xc}[n(\mathbf{r})]$, has also been introduced which is defined as,

$$\mathscr{E}_{xc}[n(\mathbf{r})] = T[n(\mathbf{r})] - T_s[n(\mathbf{r})] + V[n(\mathbf{r})] - \frac{1}{2}\int \frac{n(\mathbf{r})n(\mathbf{r}')}{|\mathbf{r}-\mathbf{r}'|}\mathrm{d}\mathbf{r}\mathrm{d}\mathbf{r}'. \tag{5.6}$$

The functional derivative of this energy is denoted, $V_{xc}[n(\mathbf{r})]$, and referred to as the XC potential. The effective potential is now found by calculating the functional derivative of the energy functionals and comparing the results, the derivatives are given by

$$\begin{aligned}
\frac{\delta\mathscr{E}_s[n(\mathbf{r})]}{\delta n(\mathbf{r})} &= \frac{\delta T_s[n(\mathbf{r})]}{\delta n(\mathbf{r})} + V_{\text{eff}}(\mathbf{r}) \\
\frac{\delta\mathscr{E}[n(\mathbf{r})]}{\delta n(\mathbf{r})} &= \frac{\delta T_s[n(\mathbf{r})]}{\delta n(\mathbf{r})} + V_{\text{ext}}(\mathbf{r}) + V_{xc}[n(\mathbf{r})] + \int \frac{n(\mathbf{r}')}{|\mathbf{r}-\mathbf{r}'|}\mathrm{d}\mathbf{r}'.
\end{aligned}$$

From these two equations it is easily seen that it is possible to map the auxiliary non-interacting system to the interacting system by setting

$$V_{\text{eff}}(\mathbf{r}) = V_{\text{ext}}(\mathbf{r}) + V_{xc}[n(\mathbf{r})] + \int \frac{n(\mathbf{r}')}{|\mathbf{r}-\mathbf{r}'|}\mathrm{d}\mathbf{r}'. \tag{5.7}$$

The last thing to note is that the energy functional of the auxiliary non-interacting system is not the same as the interacting system. Inserting Eq. (5.7) into Eq. (5.4) and matching with Eq. (5.5) we can see that we need to subtract half of the Hartree energy, and add the XC energy and subtract the integral involving the XC potential which yields the total energy as,

$$E = \sum_{k=1}^{N} \varepsilon_n - \frac{1}{2} \int \frac{n(\mathbf{r})n(\mathbf{r}')}{|\mathbf{r}-\mathbf{r}'|} \mathrm{d}r\mathrm{d}\mathbf{r}' + \mathscr{E}_{xc}[n(\mathbf{r})] - \int \mathrm{d}\mathbf{r}\, V_{xc}[n(\mathbf{r})]n(\mathbf{r}), \tag{5.8}$$

where the sum is over occupied Kohn-Sham orbitals. Hence, the many body Schrödinger equation has been transformed into a non-interacting single particle equation with an effective potential. However, we have paid a price in doing so, the effective potential depends on the density, which in turn depends on the single particle states. Therefore, we have to solve the equations self-consistently. The solution is as follows, make an initial guess of the density, calculate the effective potential Eq. (5.7) and then solve the non-interacting equation Eq. (5.3). The non-interacting equation provides us with a new set of wave functions, and from these wave functions we can calculate a new density,

$$n(\mathbf{r}) = \sum_{n=1}^{N} |\psi_n(\mathbf{r})|^2. \tag{5.9}$$

Now that we have a new density, we can repeat the process until the difference in energy, Eq. (5.8), between two successive iteration is sufficiently small. For the interested reader, excellent reviews of the DFT framework are outlined in [78–80].

Lastly, it is important to note that we moved all of our ignorance about the electron-electron interaction and the kinetic energy into one term, the XC functional, which we need an approximation for.

## 5.3 Local density approximation

In the previous section, we outlined how Kohn and Sham wrote down the fundamentals of solving the Schrödinger equation in the Born-Oppenheimer approximation. We wrote down the equations that can be used to find the ground state energy and density. However, we still have to find an approximation of the XC energy. The first devised XC energy functional, given in Eq. (5.6), is the Local Density Approximation (LDA) which assumes that the density varies slowly such that we may approximate the potential as local, i.e., it depends only on the density at $\mathbf{r}$. However, note that the true potential will be non-local and not only depend on the density at $\mathbf{r}$ but also on all other points $\mathbf{r}'$. This approximation leads to the XC energy as

$$\mathscr{E}_{xc}[n] = \int \epsilon_{xc}[n(\mathbf{r})]n(\mathbf{r})\mathrm{d}\mathbf{r}.$$

where $\epsilon_{xc}$ is the XC energy per particle of the homogeneous system with density $n(\mathbf{r})$. Even with this approximation, no analytical form of $\epsilon_{xc}$ is known. However, $\epsilon_{xc}$ can be separated into an exchange and correlation term. The exchange term is straight forward to derive, see e.g., [72]. As the name suggests, the interaction involves the exchange of two electrons, which leads to a lowering of the energy. The reduction in energy is rooted in the antisymmetrization of the wave function, which is a materialization of the Pauli exclusion principle. The antisymmetrization keeps electrons with parallel spin apart. Therefore, the effect of the exchange term can be though of as every spin up (spin down) electron having a small bubble of deficient spin up (spin down) that follows the electron around, this effect is called the *exchange hole*. The lowering of the energy can thus be interpreted as the interaction of the electron with the positive *exchange hole* surrounding it [81].

However, in the exchange energy, all other interactions have been ignored. These interactions are collectively called correlation. The correlation energy also lowers the energy, and one can think of a *correlation hole* similarly to the *exchange hole*. In addition to keeping electrons of the same spin apart, the *correlation hole* keeps electrons of antiparallel spins apart as well. It is evident that the correlation is much more important for antiparallel spins than for parallel spins, which are mostly covered by the exchange energy. Analytic expression for the correlation energy can be calculated at low and high density limits [82–84], but there exist no analytical form in between the two limits. For typical solids, the correlation energy is much smaller than the exchange energy, however, as the density decreases the correlation energy becomes more important and even dominates for very low densities.

Different parametrizations of the XC energy have been suggested based on the derived exchange and correlation energy. However, most of them are founded on the diffusion Monte Carlo calculations by Ceperley and Alder [85], which are numerically exact. Moreover, a neat detail of the diffusion Monte Carlo simulations is that they include the kinetic energy, which there exist no analytic expression for, except for a few limited cases, such as the free electron gas. Finally, despite the simplicity of LDA very accurate results have been obtained in, e.g., metallic systems where the density does not vary rapidly. The expressions for the XC energy is readily available in, e.g., Ref. [72].

## 5.4 Generalized gradient approximation

A natural extension to the LDA is to include derivatives of the density, which should better account for the density variations found in real materials. This family of functionals is termed, Generalized gradient approximation (GGA). The exchange correlation energy is then written as,

$$\mathcal{E}_{xc}[n] = \int f[n(\mathbf{r}), \nabla n(\mathbf{r})] \mathrm{d}\mathbf{r}.$$

Unintuativley, inclusion of the gradient initially made the results worse. However, inclusions of constraints such as, e.g., sum rules and known features about the *exchange* and *correlation hole* resulted in satisfactory functionals. One such functional and probably the most widely used in materials science is the PBE functional parametrized by Perdew, Burke and Ernzerhof [86].

The GGAs can also be parametrized by empirical fitting to known experimental results. However, this leads to poor transferability, and it is not obvious that the experimental results are reproduced due to the correct physics. An excellent discussion on the empirical vs constrained parametrization can be found in Ref. [87].

## 5.5 DFT + U

The Hartree term introduced in the exchange correlation functional, Eq. (5.6), is unphysical in a sense, the electron interacts with a density which itself is a part of. In theory, this interaction should be completely corrected for if we had a complete description of the XC functional. However, since we only have approximations of it, we are left with an issue, the electron interacts with itself. The self interaction, leads to an over-delocalization of the electrons. Corrections to the self interaction can, e.g., improve the predicted band gaps [88]. But, despite the improved band gap with self interaction corrections, it has been argued that the band gap problem would not be solved even with an exact XC description. Rather, one would have to go beyond DFT to solve the problem [89]. The band gap problem is thoroughly discussed in, e.g., Ref. [90].

One way of treating the over-delocalization issue known to LDA and the GGAs is DFT + U. The method stems from the Hubbard model, which is an approximate model that is used to describe the phase transition from metal to insulator of a solid-state system. The model Hamiltonian is written as,

$$\mathscr{H} = -t \sum_{\langle AB\rangle,\sigma} (c^{\dagger}_{A\sigma} c_{B\sigma} + c^{\dagger}_{B\sigma} c_{A\sigma}) + U \sum_{i} c^{\dagger}_{i\uparrow} c_{i\uparrow} c^{\dagger}_{i\downarrow} c_{i\downarrow}$$

where the first term is the hopping of the electrons between sites, $\langle AB\rangle$ indicates that it is a sum over nearest neighbor pairs A and B. The second part represent the electron-electron repulsion and is important for strongly correlated materials, i.e., there is an associated cost of placing electrons on the same site. The transfer, or hopping integral, t, is related to the crystal potential and kinetic energy as,

$$t = \int \mathrm{dr}\, \psi^{*}_{A}(\mathbf{r}) \left[-\frac{1}{2m}\nabla^{2} + V(\mathbf{r})\right] \psi_{B}(\mathbf{r}).$$

Incorporating this formalism in DFT then gives the energy functional as [91],

$$\mathscr{E} = \mathscr{E}_{\mathrm{DFT}} + \frac{U_{\mathrm{eff}}}{2} \sum_{\sigma} Tr(\rho_{\sigma}) - Tr(\rho_{\sigma}\rho_{\sigma}),$$

where $\rho_\sigma$ is the atomic orbital occupation matrix. In the solid-state community the occupation matrix is commonly calculated by projecting the plane waves onto a localized basis set [92]. The interaction will force the orbital to either be fully occupied or fully unoccupied.

A significant benefit of the DFT + U formalism is that it does not significantly increase the computational time. However, the model is not transferable between systems since the U parameter is system dependent. That is, there is no "universal" way of determining a U parameter that should be suitable for all materials. However, there are ways of determining it theoretically for a specific system, see e.g., Ref. [92, 93]. For an excellent in depth review of the DFT + U approach, see, e.g., Ref. [92].

## 5.6 Hybrid functionals

A more system independent way of treating the known over-delocalization of the electrons in DFT is to incorporate exact exchange [94]. The idea is that, if we incorporate some exact exchange energy from the Hartree-Fock theory, we can correct for the over-delocalization of e.g., LDA or the GGAs. The exact exchange energy is given by [95],

$$\mathscr{E}_x^{\mathrm{HF}} = \sum_{ab} f_a f_b \int \mathrm{d}^3\mathbf{r}'\, \mathrm{d}^3\mathbf{r}\, \frac{\psi_a^*(\mathbf{r})\psi_b^*(\mathbf{r})\psi_b(\mathbf{r}')\psi_a(\mathbf{r}')}{|\mathbf{r}-\mathbf{r}'|} \tag{5.10}$$

where $f_a$ and $f_b$ is the occupation of orbital a and b. The energy functional that is used in, e.g., PBE0 [94], which is a hybrid functional is then defined as,

$$\mathscr{E} = \frac{1}{4}\mathscr{E}_x^{\mathrm{HF}} + \frac{3}{4}\mathscr{E}_x^{\mathrm{PBE}} + \mathscr{E}_c^{\mathrm{PBE}}.$$

The fraction of mixing, ¼, of the exact exchange has been determined theoretically. The orbital dependence in Eq. (5.10) leads to a significant increase in computational time. To reduce the computational time for extended systems but still maintain good accuracy, it has been suggested that the Coulomb kernel can be separated into a long range and short range part. One such functional is HSE06 [96] where the Coulomb kernel is separated in the following way,

$$\frac{1}{|\mathbf{r}-\mathbf{r}'|} = \frac{\mathrm{erf}(\mu|\mathbf{r}-\mathbf{r}'|)}{|\mathbf{r}-\mathbf{r}'|} + \frac{\mathrm{erfc}(\mu|\mathbf{r}-\mathbf{r}'|)}{|\mathbf{r}-\mathbf{r}'|},$$

$\mu$ controls the screening, and is given by 0.2 for HSE06. The first term is then the short range part , and the second term is the long range part. The energy functional is then given as,

$$\mathscr{E} = \frac{1}{4}\mathscr{E}_x^{\mathrm{HF,SR}} + \frac{3}{4}\mathscr{E}_x^{\mathrm{PBE,SR}} + \mathscr{E}_x^{\mathrm{PBE,LR}} + \mathscr{E}_c^{\mathrm{PBE}}.$$

## 5.7 Basis functions and pseudopotentials

In practice, the wave functions in the Kohn-Sham equation Eq. (5.3) can be found by solving the equation on a grid. However, for extended systems such as the systems in this thesis, this method would be computational impractical. Instead, a basis set is introduced such that the wave functions can be represented as,

$$\Psi_i(r) = \sum_j c_{ij}\phi_j,$$

where $\phi_j$ can be chosen in a few different ways. The introduction of the basis functions maps a continuous problem into a problem of linear algebra. Therefore, the problem reduces to finding the expansion coefficients $c_{ij}$. The choice of basis function depends on the problem, a natural choice for extended periodic systems is, e.g., plane waves,

$$\Psi_{i,\mathbf{k}}(r) = \sum_{\mathbf{G}} c_{i,\mathbf{k}}(\mathbf{G}) \exp\left(i\mathbf{r}\cdot(\mathbf{k}+\mathbf{G})\right),$$

where the periodicity is implicitly implied. Plane waves form a complete basis, however, for practical calculation we have to truncate the expansion at some point. This is done via the kinetic energy, $\frac{1}{2}|\mathbf{k}+\mathbf{G}|^2 < E_{\mathrm{cut}}$, such that all plane waves fulfilling the criteria are included. It is thus straight forward to increase the size of the basis set and thus increase the accuracy of the calculation.

Unfortunately, the orthogonality requirement of the wave functions leads to rapid oscillations in the core region of the valance electrons. Consequentially, the kinetic energy of the valance electrons will be large, and by necessity a sizable $E_{\mathrm{cut}}$ has to be chosen. A computational tractable way to handle the rapid oscillations is to introduce a pseudopotential [97]. The idea is to construct a pseudowave function where the rapid oscillations of the valance states in the core region has been removed. Moreover, by construction, these pseudowave functions ensures that the valance states remain orthogonal to the core states. Furthermore, given that the pseudopotential is carefully constructed, the correct energy eigenvalues should be obtained.

Exactly how the pseudopotential is constructed varies. For example, how many states that are treated as core states and how large the core radius is can vary depending on the application. Usually, a few different potentials are constructed, and the user decided which potential to use based on the accuracy required. The only necessity is that the pseudopotential should be constructed such that the pseudowave function coincides with the true wave functions outside the core region. Therefore, a few different implementations of pseudopotentials have been proposed such as norm-conserving, ultrasoft and projector augmented wave (PAW) potentials [98–100]. The PAW method allows us to reconstruct the true wave function in the core region, and this is also the formalism together with plane waves that has been employed in all the DFT calculations in this thesis.

# 6

# Vibrational motion

In this chapter, we will discuss the atomic motion, the motion of the nuclei. The Hamiltonian is given by,

$$\mathscr{H} = \sum_i \frac{\mathbf{P}_i^2}{2m_i} + V(\ldots, \mathbf{R}_i, \ldots) \tag{6.1}$$

where $\mathbf{P}_i$ is the momentum, $m_i$ the mass and $\mathbf{R}_i$ the position coordinate of atom $i$. It is convenient to write the atomic positions as,

$$\mathbf{R}_i = \mathbf{R}_i^0 + \mathbf{u}_i, \tag{6.2}$$

where $\mathbf{R}_i^0$ is the equilibrium position and $\mathbf{u}_i$ the displacement from the equilibrium position.

## 6.1 Force constants

The potential energy $V(\ldots, \mathbf{R}_i, \ldots)$ in Eq. (6.1) can be expanded as a Taylor series,

$$V = V_0 + \Phi_i^\alpha u_i^\alpha + \frac{1}{2!}\Phi_{ij}^{\alpha\beta} u_i^\alpha u_j^\beta + \frac{1}{3!}\Phi_{ijk}^{\alpha\beta\gamma} u_i^\alpha u_j^\beta u_k^\gamma + \ldots \ , \tag{6.3}$$

where Einstein summation applies and the $\Phi$s are referred to as force constants (FC). Latin indices run over atomic labels and Greek letters run over Cartesian coordinates. The first term, $V_0 = V_0(\ldots, \mathbf{R}_i^0, \ldots)$, is the energy at the equilibrium positions and can be obtained from, e.g., a DFT calculation. Here, we will set this reference energy equal to zero. Moreover, since we are expanding around the equilibrium positions, the second term is zero by construction. The equilibrium positions may, however, correspond to a saddle point configuration, not necessarily a minimum, but also in that case, the second term is zero. Construction of models can then be done based on third and higher terms. Finally, the FCs are defined as derivatives of the potential with respect to the displacements,

$$\Phi_i^\alpha = \frac{\partial V}{\partial u_i^\alpha}, \quad \Phi_{ij}^{\alpha\beta} = \frac{\partial^2 V}{\partial u_i^\alpha \partial u_j^\beta}, \quad \ldots,$$

and the atomic forces $F_i^\alpha$ can be written in terms of the FCs as,

$$F_i^\alpha = -\frac{\partial V}{\partial u_i^\alpha} = -\Phi_{ij}^{\alpha\beta} u_j^\beta - \frac{1}{2}\Phi_{ijk}^{\alpha\beta\gamma} u_j^\beta u_k^\gamma - \ldots. \tag{6.4}$$

### 6.1.1 Extracting force constants

A common approach to extract the harmonic FC is to use finite displacements, the frozen phonon method. That is, you displace one atom at the time and calculate the FC as [101],

$$\Phi_{ij}^{\alpha\beta} = -\frac{F_i^\alpha}{\Delta u_j^\beta}, \tag{6.5}$$

where then $\Delta u_j^\beta$ is the finite displacement of atom $j$ in direction $\beta$. The extension to higher orders is straightforward, but the number of calculations needed grows quickly. This method also becomes increasingly inefficient as the symmetry decreases or the size of the system increases.

A more computationally tractable method is to displace all atoms in the cell and recast equation (6.4) into a regression problem,

$$\mathbf{A\Phi} = \mathbf{F}, \tag{6.6}$$

where $\mathbf{A}$ is the design matrix that encodes all displacements, $\mathbf{F}$ are the corresponding forces and $\mathbf{\Phi}$ is a vector of the FCs. HIPHIVE[102] can be used to construct the regression problem, where the underlying symmetry of the system is utilized to reduce the number of independent FCs. To minimize the number of reference calculations and getting physical FCs, we want the regression problem (6.6) to be as well posed as possible. That is, we want the structures to be as uncorrelated as possible, and hopefully have displacement patterns that are highly probable. In theory, the sum in Eq. (6.4) is infinite. Fortunately, the Taylor expansion can commonly be truncated at relatively low expansion order. Moreover, the interactions usually decay rapidly with increasing distance and number of bodies involved. Therefore, only a limited number of FCs needs to be considered in the regression problem.

## 6.2 Harmonic approximation

The *harmonic approximation* is obtained by truncating the expansion in Eq. (6.3) at the second order term,

$$V = \frac{1}{2}\Phi_{ij}^{\alpha\beta} u_i^\alpha u_j^\beta .$$

The coupled dynamics of the displacements $u_i^\alpha$ can then be transformed into a set of *independent* collective harmonic oscillators, often denoted *normal modes*, by diagonalising the force constant matrix $\Phi_{ij}^{\alpha\beta}$.

### 6.2.1 Normal modes

We are considering crystalline solids, where the atoms are arranged in an ordered microscopic structure, forming a crystal lattice that extends in all directions. A *unit cell* is introduced, containing $n_a$ atoms, which is repeated periodically in all three directions. The dynamics of the system can then be solved in reciprocal space, q-space, by solving the eigenvalue equation [72],

$$D(\mathbf{q})\,\mathbf{e}_{\mathbf{q}\nu} = \omega_{\mathbf{q}\nu}^2\,\mathbf{e}_{\mathbf{q}\nu}, \tag{6.7}$$

where $D(\mathbf{q})$ is the dynamical matrix, $\omega_{\mathbf{q}\nu}$ the frequency, and $\mathbf{e}_{\mathbf{q}\nu}$ the corresponding eigenvector, or normal mode coordinate. The size of the dynamical matrix is $3n_a \times 3n_a$ and the eigenvalue equation has to be solved for each $\mathbf{q}$ vector in the Brillouin zone, the unit cell in reciprocal space. The index $\nu = 1, \ldots, 3n_a$ is called the branch index. More explicitly, the dynamical matrix can be written as

$$D_{\kappa\kappa'}^{\alpha\beta}(\mathbf{q}) = \sum_{l'} \frac{\Phi_{0\kappa;l'\kappa'}^{\alpha\beta}}{\sqrt{m_\kappa m_{\kappa'}}} \exp\left[-i\mathbf{q}\cdot\left(\mathbf{R}_{0\kappa}^0 - \mathbf{R}_{l'\kappa'}^0\right)\right]. \tag{6.8}$$

The atomic index $i$ has here been decomposed as $i = (l\kappa)$, where $l$ and $\kappa$ are labels of unit cells and atoms in each unit cell, respectively.

The frequencies obtained in the diagonalization of the dynamical matrix are commonly presented in a density of states (DoS) figure. The DoS,

$$g(\omega) = \frac{1}{N_q}\sum_{\mathbf{q}\nu} \delta(\omega - \omega_{\mathbf{q}\nu}), \tag{6.9}$$

counts the number of states available at a given frequency. We have, here divided with $N_q$, the number of $\mathbf{q}$-points in the summation. This implies that $g(\omega)$ is normalized such that the integration over frequency becomes $3n_a$. We can also determine the density of states of a single atomic type,

$$g_A(\omega) = \frac{1}{N_q}\sum_{\mathbf{q}\nu} c_A(\mathbf{q},\nu)\delta(\omega - \omega_{\mathbf{q}\nu})$$

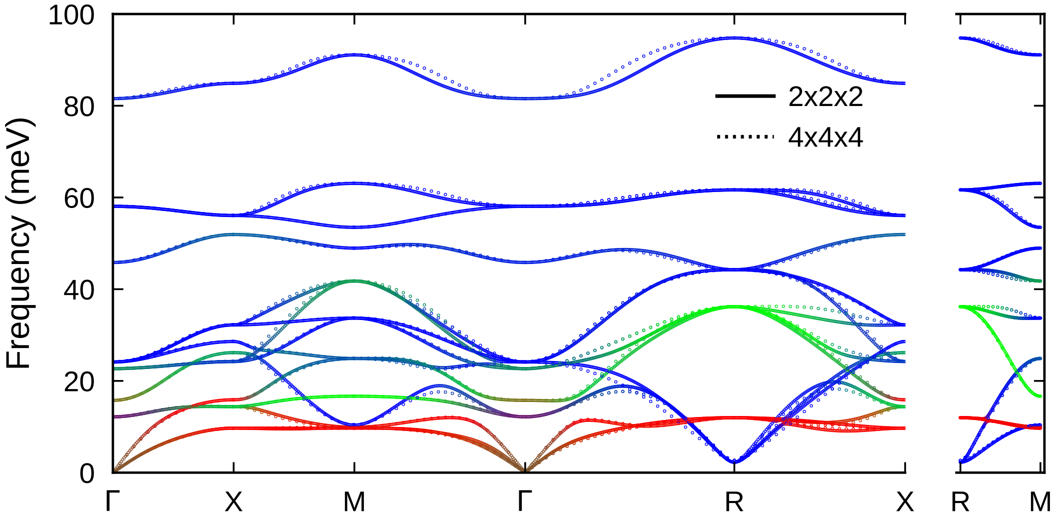

**Figure 6.1**: Phonon dispersion for BZO using PBE. Data are shown between high symmetry points and are derived using PHONOPY for a $2 \times 2 \times 2$ and a $4 \times 4 \times 4$ supercell, respectively. Color assigned as (Ba, Zr, O) = (R, G, B).

where

$$c_A(\mathbf{q}, \nu) = \sum_{i \in A} \sum_{\alpha} |\hat{\mathbf{n}}_{i\alpha} \cdot \mathbf{e}_{\mathbf{q}\nu}|^2$$

is how much atomic type A contributes to the normal mode. Here $\hat{\mathbf{n}}_{i\alpha}$ is a unit projection vector of atom i in direction $\alpha$ and the sum over $i$ is taken over all atoms of type A.

The frequency along the paths between the high symmetry points in the Brillouin zone can be plotted in what is referred to as a dispersion plot. This is shown in Fig. 6.1 for BZO using the PBE functional. The unit cell (5 atoms) is cubic with size $a_0$=4.24 Å and the calculations are done using PHONOPY. For definition of the high symmetry points, see Fig. 2.1. The color coding is (Ba, Zr, O) = (R, G, B), which implies that, e.g., a pure oxygen mode will be colored blue and mixed modes will have a mixed color. The direct method introduced by Parlinski *et al.* [103] is used with individual atomic displacements with size 0.01 Å. The size of the computational cell, the supercell, is 2x2x2 of the unit cell and the LO-TO splitting is included following Ref. [104]. The direct method in Ref. [103] will give the exact frequencies at high symmetry points, due to the use of the 2x2x2 supercell. Interpolation between these high symmetry points is carried out and if the range of the physical interaction is within half of the supercell size, then the interpolation scheme gives the correct frequencies also in between the high symmetry point.

To test the accuracy with respect to the range of the physical interaction between the atoms we have also done the calculations for a 4x4x4 supercell. The result is shown as dotted lines in Fig. 6.1. The two calculations agree at the high symmetry points and in between the differences are only a few meV. We conclude that a supercell with size 4x4x4 should be sufficient with respect to range of the physical interaction.

### 6.2.2 Thermodynamics and phonons

The thermal properties of the vibrational motion can be obtained from statistical mechanics. The motion is quantized and the normal mode becomes a quasiparticle, a *phonon*. The canonical partition function for the phonon system is given by [105]

$$Z = \prod_{\mathbf{q}\nu} \frac{\exp\left(-\beta\hbar\omega_{\mathbf{q}\nu}/2\right)}{1-\exp\left(-\beta\hbar\omega_{\mathbf{q}\nu}\right)}. \tag{6.10}$$

where $\beta = 1/k_B T$. The energy is then given by

$$\begin{aligned} U(T) &= -\frac{\partial}{\partial\beta}\ln Z \\ &= \sum_{\mathbf{q}\nu}\left(\frac{1}{2}+\frac{1}{\exp\left(\beta\hbar\omega_{\mathbf{q}\nu}\right)-1}\right)\hbar\omega_{\mathbf{q}\nu} \end{aligned} \tag{6.11}$$

and by using the expression for the density of states in Eq. (6.9) the sum can be replaced by an integral

$$\begin{aligned} U(T) &= \int_0^\infty g(\omega)\,\mathrm{d}\omega\left(\frac{1}{2}+\frac{1}{\exp\left(\beta\hbar\omega\right)-1}\right)\hbar\omega \\ &= \int_0^\infty g(\omega)\,\mathrm{d}\omega\left(\frac{1}{2}+\langle n(\omega,T)\rangle\right)\hbar\omega\,. \end{aligned} \tag{6.12}$$

In the last line the Bose-Einstein distribution $\langle n(\omega,T)\rangle$ is introduced, the mean occupancy of the state with frequency $\omega$ at temperature $T$. In the same way the entropy is given by

$$\begin{aligned} S(T) &= -k_\mathrm{B}\,\beta^2\frac{\partial}{\partial\beta}\left(\frac{1}{\beta}\ln Z\right) \\ &= k_\mathrm{B}\int_0^\infty g(\omega)\,\mathrm{d}\omega\left(\frac{\beta\hbar\omega}{\exp\left(\beta\hbar\omega\right)-1}-\ln\left(1-\exp\left(-\beta\hbar\omega\right)\right)\right)\,. \end{aligned} \tag{6.13}$$

and the Helmholtz free energy $F$ is then obtained from the relation

$$F(T) = U(T) - TS(T)\,. \tag{6.14}$$

In Fig. 6.2 the computed temperature dependence for the energy, entropy and free energy for BZO using PBE is depicted. The energy and entropy increases as function of temperature, while the free energy decreases.

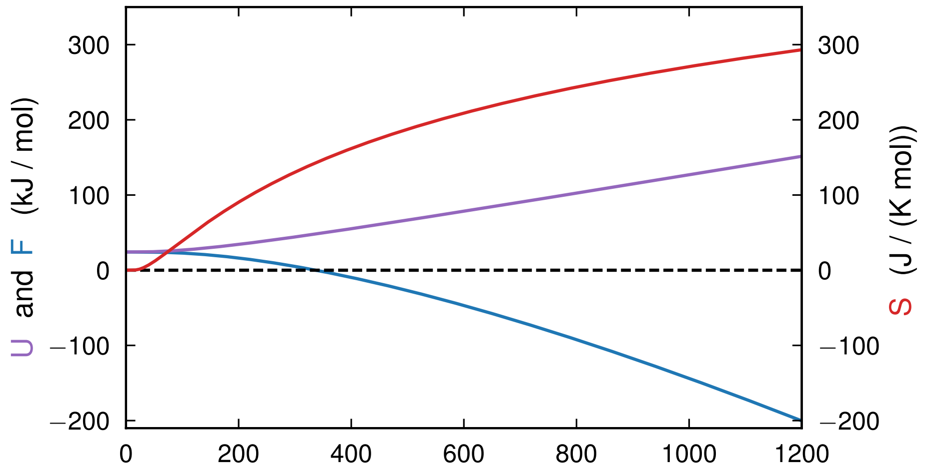

**Figure 6.2:** The thermal energy $U$, entropy $S$ and free energy $F$ as function of temperature for BZO.

#### 6.2.2.1 Mean-squared displacement

The atomic displacement operator can be expressed as [101],

$$\hat{u}_i^\alpha = \frac{1}{N_q}\sum_{\mathbf{q}\nu}\sqrt{\frac{\hbar}{2m_i\omega_{\mathbf{q}\nu}}}\left(a_{\mathbf{q}\nu}+a^\dagger_{-\mathbf{q}\nu}\right)\exp\left[i\mathbf{q}\cdot\mathbf{R}_i^0\right]\left(\hat{\mathbf{n}}_{i\alpha}\cdot\mathbf{e}_{\mathbf{q}\nu}\right) \tag{6.15}$$

where $a^\dagger$ and $a$ is the creation and annihilation operators [72]. The distribution of the atomic displacements can then be obtained as expectations values of Eq. (6.15). It can be shown [106] that the distribution is an uncorrelated multivariate Gaussian in *phonon* coordinates, or **q**-space. The mean value is zero and the variance is given by the mean-squared displacement (MSD),

$$\left\langle (u_i^\alpha)^2\right\rangle(T) = \frac{1}{N_q}\sum_{\mathbf{q}\nu}\frac{\hbar}{m_i\omega_{\mathbf{q}\nu}}\left[\frac{1}{2}+\langle n(\omega_{\mathbf{q}\nu},T)\rangle\right]\left(e^{i\alpha}_{\mathbf{q}\nu}\right)^2 \tag{6.16}$$

where $e^{i\alpha}_{\mathbf{q}\nu} = |\hat{\mathbf{n}}_{i\alpha}\cdot\mathbf{e}_{\mathbf{q}\nu}|$. Ref. [107] shows that the distribution in atomic displacements is a correlated multivariate Gaussian with zero mean. In the classical limit the MSD becomes proportional to temperature,

$$\left\langle (u_i^\alpha)^2\right\rangle(T\to\infty) = \frac{1}{N_q}\sum_{\mathbf{q}\nu}\frac{k_BT}{m_i\omega^2_{\mathbf{q}\nu}}\left(e^{i\alpha}_{\mathbf{q}\nu}\right)^2, \tag{6.17}$$

while at low temperatures it approaches the zero-point motion value

$$\left\langle (u_i^\alpha)^2\right\rangle(T=0) = \frac{1}{N_q}\sum_{\mathbf{q}\nu}\frac{\hbar}{2m_i\omega_{\mathbf{q}\nu}}\left(e^{i\alpha}_{\mathbf{q}\nu}\right)^2. \tag{6.18}$$

## 6.3 Sampling configurational space

In extracting, FC one can make use of the frozen phonon method and displace one atom at the time. However, here we will consider the more efficient method and directly displace all atoms in the cell and thereby collecting training structures for the regression problem in Eq. (6.6). For instance, one can displace all atoms according to a normal distribution given some appropriate standard deviation. This method has been denoted Rattle [102].

A more proper, but also more computationally demanding way of generating the training structures, is to generate displacements using molecular dynamics (MD), preferably ab-initio molecular dynamics (AIMD).

Another attractive way to generate training structures is to make use of derived normal modes. The normal modes can be populated according to some given temperature. To generate the atomic displacements, which are Gaussian distributed, the Box-Muller method can be used. The displacements are then given by

$$u_i^\alpha = \sum_\nu A_\nu^i e_\nu^{i,\alpha} \sqrt{-2\ln(Q_\nu)}\cos(\pi U_\nu), \tag{6.19}$$

where $Q_\nu$ and $U_\nu$ are two uniform random numbers between 0 and 1, and

$$A_\nu^i = \left[\frac{\hbar}{m_i\omega_\nu}\left(\frac{1}{2} + n(\omega_\nu, T)\right)\right]^{1/2}. \tag{6.20}$$

We have here dropped the index $\mathbf{q}$, since we are only interested in the modes that are commensurate with the supercell, the modes at the $\Gamma$-point for the supercell. If we would like to populate the modes classically instead, the amplitude

$$A_\nu^i = \left[\frac{k_B T}{m_i\omega_\nu^2}\right]^{1/2} \tag{6.21}$$

should be used.

In Fig. 6.3 we show results for BZO using the "standard" method based on individual atomic displacements with size 0.01 Å (here denoted PHONOPY) and using the method based on training structures and regression (here denoted HIPHIVE). The PHONOPY results are the same as in Fig. 6.1 and the HIPHIVE results are based on training structures from phonon modes at 100 K using the classical amplitude in Eq. (6.21). Both results are based on a 4x4x4 supercell and in the HIPHIVE calculations the cutoff for the FCs is set to 8.0 Å, about $L/2$, where $L = 4a_0 = 16.94$ Å is the supercell size. In the same figure we show the projected DoS which is smeared using a Gaussian kernel with $\sigma = 0.2$ meV.

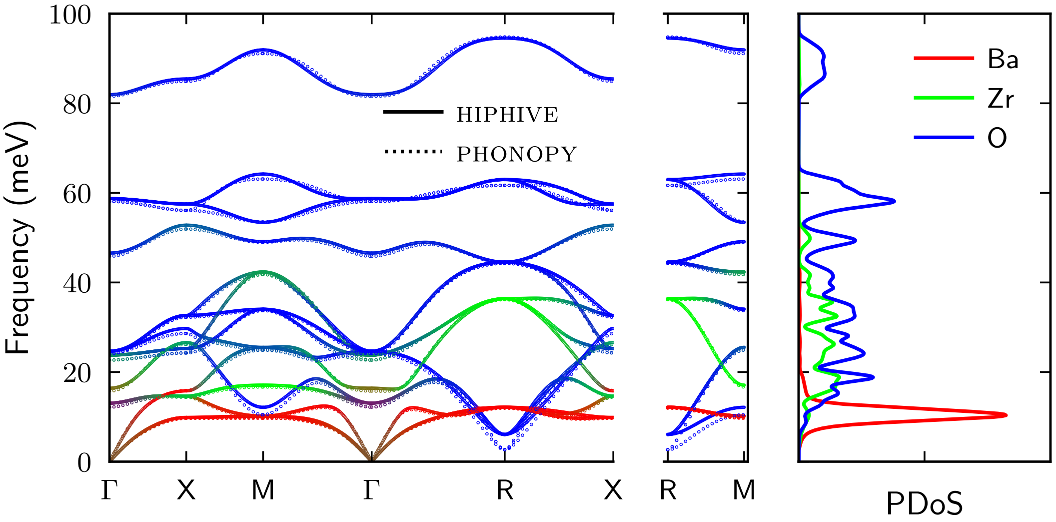

**Figure 6.3:** projected dispersion at the high symmetry points using HIPHIVE and PHONOPY in the $4 \times 4 \times 4$ supercell. Color assigned as (Ba, Zr, O) = (R, G, B).

We notice that the two methods give very similar results. There is, however, a difference for the lowest mode at the R point. That motion is strongly anharmonic, leading to a *renormalized* larger frequency for the HIPHIVE method. This is owing to the larger and more physical displacements that are sampled by that method.

## 6.4 Anharmonicity

The harmonic model provided equations for calculating frequencies, and, e.g., free energies. However, there are a lot of properties of a material that are related to the lattice that are not described by the harmonic approximation. For example, lattice thermal conductivity, thermal expansion, phonon lifetimes, soft modes and structural phase transitions [101, 108, 109]. Higher order terms from the expansion in Eq. (6.3), then have to be included. Keeping terms up to fourth order gives us,

$$V = \frac{1}{2!}\Phi_{ij}^{\alpha\beta}u_i^\alpha u_j^\beta + \frac{1}{3!}\Phi_{ijk}^{\alpha\beta\gamma}u_i^\alpha u_j^\beta u_k^\gamma + \frac{1}{4!}\Phi_{ijkl}^{\alpha\beta\gamma\upsilon}u_i^\alpha u_j^\beta u_k^\gamma u_l^\upsilon. \tag{6.22}$$

Therefore, it is apparent that we need methods that also address the anharmonic interactions.

### 6.4.1 Perturbation theory

The dynamics of the anharmonic system can be investigated by, e.g., perturbation theory. This is carried out by writing the harmonic Hamiltonian on a diagonal form using the creation and annihilation operators [108],

$$\mathscr{H} = \sum_{\lambda} \hbar\omega_{\lambda} \left( a_{\lambda}^{\dagger} a_{\lambda} + \frac{1}{2} \right), \tag{6.23}$$

with energy eigenstates, $|n\rangle$, sometimes referred to as Fock states. The displacement operator, defined Eq. (6.15), was used to rewrite the Hamiltonian and $\lambda = (\mathbf{q}, \nu)$. A potential of the third order can then be written as [108],

$$\mathscr{H}_3 = \sum_{\lambda\lambda'\lambda''} \Psi_{\lambda\lambda'\lambda''} (a_{\lambda} + a_{-\lambda}^{\dagger})(a_{\lambda'} + a_{-\lambda'}^{\dagger})(a_{\lambda''} + a_{-\lambda''}^{\dagger}), \tag{6.24}$$

where the same displacement operator is used and $-\lambda = (-\mathbf{q}, \nu)$. Extension to even higher orders is straight forward. The potential in Eq. (6.24) will cause scattering between the Fock states as, $\mathscr{H}_3$ contains terms such as, $a_{\lambda}^{\dagger} a_{\lambda'} a_{\lambda''}^{\dagger}$. As a result, the Fock states are no longer energy eigenstates of the Hamiltonian. One way to handle this issue is to use perturbation theory, given that the anharmonicity is weak.

Maradudin and Fien [110] have an excellent discussion of how the anharmonic system impacts the frequency of the system using perturbation theory. They showed that the unperturbed system, the harmonic system, will experience a complex shift of the frequency, $\Delta\omega + i\Gamma$. The imaginary part ($\Gamma$) is related to the lifetime of the phonons, which leads to a broadening of the vibrational spectrum, which we will see later. The $\Delta\omega$ is simply a shift of the frequency. Ref. [108] uses perturbation theory to calculate $\Gamma$ using a third order potential for a couple of different materials.

### 6.4.2 Quasi harmonic approximation

The simplest correction to the real part of the complex shift is due to the increased (or decreased) separation of the nearest neighbor atoms at elevated temperatures, thermal expansion. The thermal expansion can be calculated directly from higher order derivatives of the PES as presented in [110], or by explicitly changing the volume and calculate a new set of frequencies, which is done in the quasi harmonic approximation [101]. Practically, this carried out by calculating the harmonic frequencies and electronic energies at a few different volumes, and then minimizing the free energy with respect to the volume at different temperatures. It is evident that the electronic energies increase with either an increase or decrease in volume. However, the frequencies are commonly decreasing with increasing volume as the bonds tends to soften. This increases the vibrational entropy, and in turn decreases the free energy, which leads to an expansion of the volume. It is worth noting that there exists materials with negative thermal expansion, but they are rare, see e.g., [111].

### 6.4.3 Soft modes and structural phase transitions

As noted in the beginning of this chapter, it is not given that the potential was expanded around a minimum, it could as easily have been expanded around a saddle point (or a local maximum). That is, we know that the Jacobian is zero, however, for a minimum it is required that the Hessian matrix should be positive definite, that is, all eigenvalues are positive. Therefore, if the dynamical matrix, Eq. (6.7), which is related to the Hessian, exhibits negative eigenvalues we conclude that the potential was not expanded around a minimum but rather at a saddle point. This means that the potential energy is lowered along the normal mode corresponding to that eigenvalue.

Structures that exhibit negative eigenvalues of the dynamical matrix are sometimes referred to as *dynamically unstable* structures. However, at elevated temperatures, experiments might indicate that the *dynamically unstable* structure is the one that is observed. For example, BCO undergoes a series of phase transitions from orthorhombic to rhombohedral to cubic. However, the dynamical matrix of the cubic and rhombohedral structure exhibits negative eigenvalues (imaginary frequencies) [112]. The explanation is that the anharmonic forces can stabilize the structure. Moreover, if the anharmonic interactions are very strong, the real part of the complex shift for the frequency might be large. Modes with large shifts of the frequency with respect to the temperature are sometimes referred to as soft modes.

## 6.5 Effective harmonic modelling

The idea behind effective harmonic modelling is to generate a harmonic model that represents the anharmonic system at a specific temperature and, if needed, volume. We will restrict the analysis to the temperature dependence, but extensions to include the thermal expansion is straight forward, although more computationally demanding. There exist a plethora of methods that implements this, see e.g., [107, 113–116]. For example, some methods include the following minimization problem,

$$\min_{\mathbf{\Phi}(\boldsymbol{T})} \left\{ \langle (\mathscr{H} - \mathbf{\Phi}(T))^2 \rangle_\lambda \right\} . \tag{6.25}$$

$\mathbf{\Phi}(T)$ is the second order FC at temperature T and $\lambda$ is the ensemble in which the minimization is carried out. While other methods rely on Green's functions [115, 116] or a variation formulation [107]. The ensemble can either be the harmonic ensemble which is generated by the model, or the anharmonic ensemble. The minimization is usually done with respect to the forces,

$$\min_{\mathbf{\Phi}} \left\{ \sum_{i\alpha} \left( F_i^\alpha - \Phi_{ij}^{\alpha\beta} u_j^\beta \right)^2 \right\} , \tag{6.26}$$

but the energy can easily be used/included if needed.

### 6.5.1 Temperature dependent effective potential

Hellman [114, 117] developed the temperature-dependent effective potential (TDEP) method. This method minimizes the difference between the harmonic model and the anharmonic system that we want to study, in the ensemble of the anharmonic system. This means that the samples, or snapshots, used in Eq. (6.26) can be, e.g., drawn from MD simulations. The minimization problem is then solved by casting the problem into a linear system of equations as discussed in Sect. 6.1 and the same methodology is employed here. A caveat of the method is that the snapshots have to be drawn sufficiently separated in time. Too frequent draws will lead to large correlations in the data, which is detrimental to the stability of the minimization problem. Other approaches based on MD simulation exists as well, see e.g., [115].

Typically, the MD simulations is carried out by AIMD, although, other methods can in principle be used too. However, if the potential is quick to evaluate, the quasiparticle concept of the phonon is likely not necessary and the dynamics of the system can be studied directly instead.

A drawback of the method is that MD simulations are classical, i.e., we have forfeited the fact that the motion of the ions should be treated quantum mechanically. However, at higher temperatures, at least above the Debye temperature, the classical treatment should be valid.

### 6.5.2 Self consistent phonons

Contrary to the TDEP method the self consistent phonon (SCPH) method minimizes the difference between the anharmonic system and harmonic model potential in the ensemble of the harmonic system. This means that, instead of MD simulations, the harmonic model is used to generate the snapshots with Eq. (6.19) for the minimization problem Eq. (6.26). The benefit of generating snapshots this way is that uncorrelated snapshots are easily generated. However, the drawback is that we need to solve the minimization problem self-consistently. Say, e.g., that your initial guess of the effective harmonic model (EHM) at the finite temperature T is generated with PHONOPY. The new model that minimizes Eq. (6.26) for the generated snapshots will be different from the PHONOPY model. Therefore, the snapshots generated from this model will be different as well. This procedure of generating snapshots and solving the minimization problem will continue until the difference between the model used to generate the snapshot and the model that solves the minimization problem has converged.

There exist a few different proposed methods that fall under the SCPH name, see e.g., Refs. [107, 113, 116]. It is worth noting that contrary to the TDEP method, it is trivial to incorporate quantum effects in the SCPH method since Eq. (6.19) with Eq. (6.20) is quantum mechanical. The effect of the quantum statistics is that, e.g., the zero point energy leads to a non-zero displacement at $T = 0\,\mathrm{K}$ and, in effect, a larger frequency

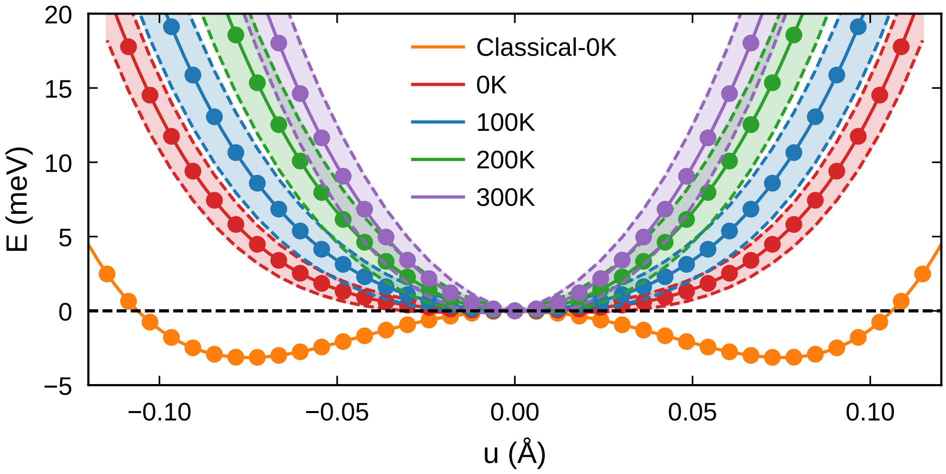

**Figure 6.4**: Temperature dependence of the tilt mode in BZO. The temperature dependence is from other thermally activated modes, and the shaded area is half the standard deviation. The underlying functional used to generate the fourth order FC potential is PBEsol.

than what is probed by e.g., TDEP at low temperatures.

#### 6.5.2.1 Effective mode potential

Fig. 6.4 shows the stabilization of the potential landscape of the AFD mode in BZO. First, note that the energy decreases along the specific mode if all other DOFs are ignored, this is marked as Classical-0K in the figure. However, a temperature can be modelled by occupying all other modes except the AFD mode at a specific temperature using Eq. (6.19) for the EHM constructed at a specific temperature. The energy of the structure is then set to zero to get a constant reference. The potential is then mapped along the mode with different amplitudes (unrelated to the temperature). The potential energy is then averaged over a large set of thermally activated structure, the shaded area is half the standard deviation. From the potential landscape, one can conclude that the zero point motion stabilizes the structure. In this case, the interpretation is that structure is unable to locate in the potential minimum, even at $T = 0\,\mathrm{K}$. However, the validity of the phonon quasi-particle close to a phase transition is poorly understood, and one should therefore be cautious in the interpretation of the results. Nevertheless, one thing is certain, the potential stiffens as the temperature is increased due to the other DOFs.

### 6.5.3 Discussion

As previously noted, the essential difference between TDEP and SCPH is in what ensemble we carry out the minimization and that it is trivial to include quantum statistics in

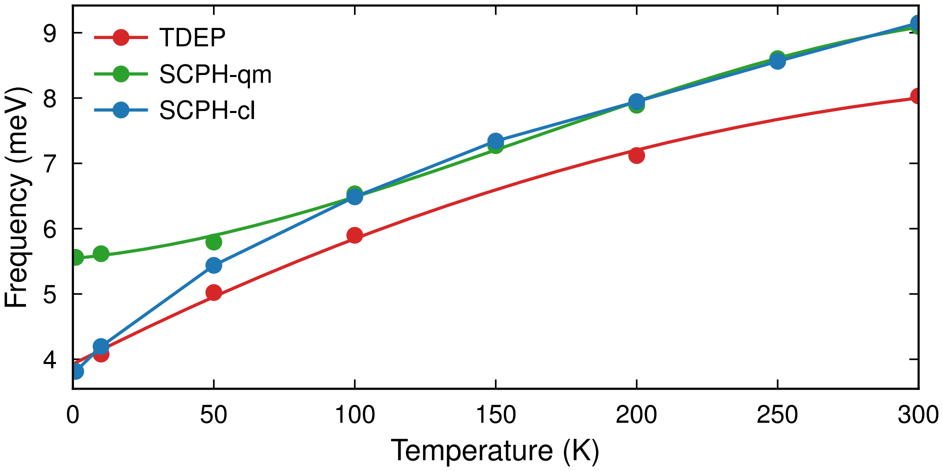

**Figure 6.5**: Temperature dependence of the frequency of the tilt mode in BZO using PBE. SCPH-cl uses the classical limit for the amplitude of the phonon while SCPH-qm uses the correct quantum amplitude.

the SCPH method. However, due to the non-interactive approximation of the phonons, it is likely that the SCPH probes higher energy parts of phase space. Nevertheless, we are trying to create an effective second order potential, not reproduce the fully anharmonic system. It is therefore not obvious which of these methods produces the best model.

Metsanurk *et al.* [118] used thermodynamic integration to discuss the errors involved in accounting for anharmonic effects in this way. The thermodynamic integration was set up such that a few values of $\lambda$ were tested in between the anharmonic and harmonic Hamiltonian. They argue that, errors in the free energy of the EHM is due to the lack of transferability. The EHM manages to describe the average potential energy in the ensemble which it was trained in. However, it fails to extrapolating to a general $\lambda$ value and therefore fails to correctly describe the actual anharmonic energies. TDEP and SCPH systematically underestimated and overestimated the average potential energy respectively for all $\lambda$s.

We tested both TDEP and SCPH to study the AFD mode in BZO with PBE. The frequency from TDEP is slightly smaller than the frequency from SCPH. A likely explanation for the higher and lower frequencies is due to the on average higher and lower potential energies compared to the actual potential found in SCPH and TDEP respectively.

Fig. 6.5 shows the calculated frequencies as a function of temperature for the two methods. SCPH-cl is the classical version of SCPH, meaning that the classical amplitude ($\hbar\omega << k_B T$) has been used in Eq. (6.19). SCPH-qm and SCPH-cl are almost completely equal at and after 100 K, however, below that temperature there is a significant difference between the two. This demonstrates the importance of accounting for the quantum motion at low temperatures.

## 6.6 Higher order models and inter-atomic potentials

By making use of the Taylor series expansion in Eq. (6.3), we can construct an inter-atomic potential with a suitable truncation of the series expansion. That is, we can fit a potential to interpolate the DFT results. However, it is important to note that the Taylor series breaks down for large displacements and is not well-defined when atoms start to diffuse. Therefore, considerable effort has been devoted to derive more general and generic inter-atomic potentials based on some modelling of the potential energy function $V(\ldots, \mathbf{R}_i, \ldots)$ in Eq. (6.1).

Behler *et al.* used neural networks [119] and Jinnouchi *et al.* used active learning [120]. These methods do not use the series expansion, but rather a different set of chemical descriptors [121]. There exist a vast number of other potential types, ATOMICREX [122], is, e.g., a software that provides a framework to construct a number of different potentials such as the embedded atom method (EAM).

The models can then be used in, e.g., MD to extract thermodynamic and dynamical properties [123]. Moreover, it is evident that you can directly use DFT, which is denoted AIMD. However, the computational cost of DFT makes, e.g., correlation functions very computational demanding.

The limitation of MD is that the motion is treated classically. Therefore, below some temperature, usually assumed to be the Debye temperature, it is questionable to run MD simulations. Below this temperature, the path integral formulation should be used to calculate, i.e., free energies, but dynamical properties are not accessible with the path integral formulation. However, centroid molecular dynamics which is based on the path integral formulation appears to give a link to correlation functions [124]. Ref. [125] uses the path integral formulation and centroid molecular dynamics to study the dynamical and static properties of quartz, and compares it to the classical dynamics.

### 6.6.1 Correlation functions and spectra

Correlation functions can be used to study the dynamics of classical systems that are strongly anharmonic. One such correlation function is the dynamical structure factor. This correlation function is also something that can be obtained from neutron scattering experiments, see, e.g., Ref. [126] for an excellent outline on how it is derived and how it relates to experiments.

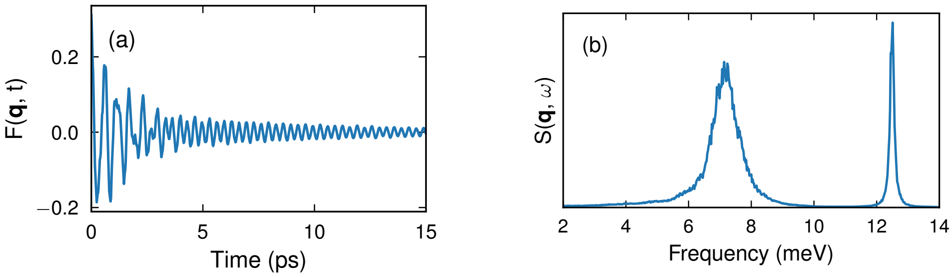

**Figure 6.6**: Result for BZO with PBE at $T = 200$ K. (a) Intermediate scattering function and (b) Dynamical structure factor.

The dynamical structure factor for atoms of type A and B,

$$S_{AB}(q,\omega) = \int_{-\infty}^{\infty} \mathrm{d}t \, \exp(-i\omega t) F_{AB}(q,t), \tag{6.27}$$

is given by the temporal Fourier transform of the intermediate scattering function,

$$F_{AB}(q,t) = \frac{1}{\sqrt{N_A N_B}} \left\langle n_A(q,t) n_B(-q,0) \right\rangle . \tag{6.28}$$

Here, $n_A(q,t)$ is the spatially Fourier transformed atomic density of atomic type A

$$\begin{aligned} n_A(q,t) &= \int \mathrm{d}\mathbf{r} \sum_A \delta(\mathbf{r} - \mathbf{R}_A(t)) \exp\left(i\mathbf{q}\cdot\mathbf{r}\right) \\ &= \sum_A \exp\left(i\mathbf{q}\cdot\mathbf{R}_A(t)\right) . \end{aligned} \tag{6.29}$$

Fig. 6.6 shows the intermediate scattering functions and the resulting dynamical structure factor for $\mathbf{q} = (2\pi/a_0)\,(2.5, 0.5, 0.5)$ at $T = 200$ K for BZO with PBE. The calculated functions are a superposition of all the individual atomic pairs, and the calculations are averaged over 20 independent MD runs. The time axis for the intermediate scattering function is shortened to 15 ps in order to show the most interesting parts, whereas the total simulation time is 100 ps. Examining the intermediate scattering function, we can clearly see a mode with a large amplitude that is heavily damped. This corresponds to the broader peak at about $\sim 7$ meV seen in the dynamical structure factor. There is also a higher frequency mode visible with smaller amplitude and lower damping. This corresponds to the more narrow peak at $\sim 12.5$ meV.

The spectrum can be fitted to the functional form derived from a damped harmonic oscillator [123],

$$f(\omega) = A \frac{\Gamma\omega_0^2}{(\omega^2 - \omega_0^2)^2 + (\Gamma\omega)^2}, \tag{6.30}$$

where $\Gamma$ is related to the phonon lifetime and $\omega_0$ is the undamped frequency. The dynamical structure factor also highlights a glaring difference between the EHM and the actual dynamics. We are trying to assign a single value, or a delta function, to a spectrum. This assignment, to me at least, is not obvious. Anecdotally, we found that the TDEP frequency compares very well with the undamped frequency of the AFD mode in BZO.

Another correlation function is the MSD, which was derived for the harmonic model and is given in Eq. (6.16). The classical limit, ($T \rightarrow \infty$), of this correlation function, can also be calculated from an MD simulations according to,

$$\Delta_i^\alpha(t) = \left\langle \left[ \mathrm{R}_i^\alpha(t+t') - \mathrm{R}_i^\alpha(t') \right]^2 \right\rangle , \tag{6.31}$$

where $\mathrm{R}_i^\alpha(t)$ is the $\alpha$-component of the position of atom $i$ at time $t$ and $\langle \ldots \rangle$ denotes a time average. For long times this will approach the classical limit of the MSD

$$\Delta_i^\alpha(t \rightarrow \infty) = 2 \left\langle (u_i^\alpha)^2 \right\rangle , \tag{6.32}$$

where for a harmonic system $\left\langle (u_i^\alpha)^2 \right\rangle$ is given by Eq. (6.17).

In Fig. 6.7 we show a comparison for MSD as function of temperature for three different models, $\mathscr{H}_2$, SCPH and MD. $\mathscr{H}_2$ is a purely harmonic model, which was constructed from the harmonic FCs of the 4th order potential. This figure highlights the difference between anharmonic and quantum effects.

Consider first the motion of oxygen perpendicular to the O-Zr bond in Fig. 6.7 (a). The vibrational frequency is low and strongly anharmonic. The corresponding displacements become large. The strong anharmonicity is evident from the deviation of SCPH from $\mathscr{H}_2$ with increasing temperature. The MD results also show a clear decrease of the slope. The low vibrational frequency implies that the motion becomes essentially

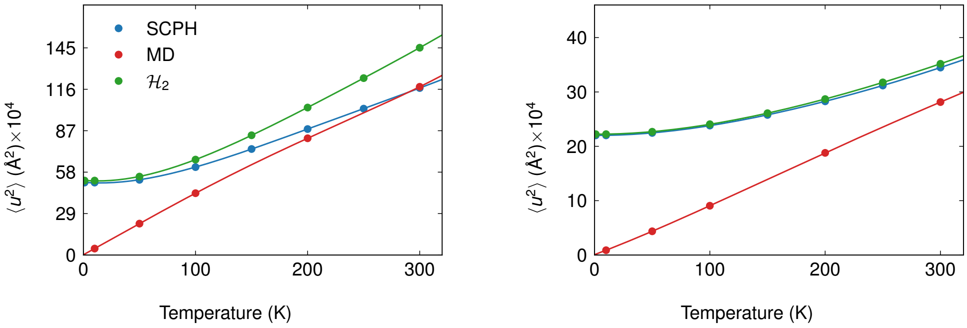

**(a)** MSD for $O \perp Zr$.

**(b)** MSD for $O \parallel Zr$.

**Figure 6.7**: The MSD calculated for BZO using PBE. We used three different models for the calculations, MD, SCPH and a purely harmonic model.

classical at 300 K, which is seen from agreement between MD and SCPH at higher temperatures.

Consider next the motion of oxygen parallel to the O-Zr bond in Fig. 6.7 (b). The vibrational frequency is high, and the corresponding displacements become small. The motion remains quantum mechanical even at 300 K and the MD results deviates from the results from the two quantum based methods, $\mathscr{H}_2$ and SCPH. However, the anharmonicity is weak and the result from $\mathscr{H}_2$ and SCPH coincide.

# 7

# Data analysis

One key aspect of data analysis is to know the biases and imperfections of your input data. This is, because, the model can only be as good as the data that it is given. It is, therefore, just as crucial to evaluate the input data as it is the final model. Moreover, solving the regression problem, Eq. (6.6), is a research field on its own, but a few straight forward solutions can easily be obtained. Therefore, in this chapter, a few key insights into how to solve Eq. (6.6), analyze the input data and evaluate the final model will be presented.

## 7.1 Regression

Regression methods estimate the relation between dependent variables, which is exactly what we are trying to do in Eq. (6.6). Below follows a few different linear regression methods.

### 7.1.1 Ordinary Least squares

The simplest solution to Eq. (6.6) is the ordinary least squares (OLS) solution which minimizes the root mean squared error (RMSE),

$$\min_{\mathbf{\Phi}} ||\mathbf{A}\mathbf{\Phi} - \mathbf{F}||_2^2. \tag{7.1}$$

Since the function is convex, it is straight forward to find the global minimum,

$$\mathbf{\Phi} = (\mathbf{A}^T\mathbf{A})^{-1}\mathbf{A}^T\mathbf{F}. \tag{7.2}$$

This solution is, however, prone to overfitting. Meaning that, if we included features in the model that are irrelevant or unimportant, they will mostly contribute to fitting noise in the input data, reducing the ability of the model to predict unseen data. The knowledge of which features are important in, e.g., the force constant expansion in Eq. (6.3) is not always self-evident and can sometimes be hard to judge prior to constructing the model, especially for higher order models. Therefore, it can be critical to use more advanced methods that remove or regularize unimportant features.

### 7.1.2 Regularization

Regularization is a class of algorithms that aims to minimize the RMSE together with a scaled penalty term, which is usually a norm of the feature vector. In Ridge ($n = 2$) and least absolute shrinkage and selection operator (LASSO) ($n = 1$), the object function is

$$\min_{\mathbf{\Phi}} \left\{ ||\mathbf{A\Phi} - \mathbf{F}||_2^2 + \lambda ||\mathbf{\Phi}||_n \right\}$$

where $||\mathbf{\Phi}||_n$ is the $\ell_n$ norm of $\mathbf{\Phi}$ and $\lambda$ is a hyperparameter. A larger $\lambda$ in LASSO leads to a sparser model (fewer features) and a smaller $\lambda$ leads to a denser model (more features). Denser models tend to describe seen data very well, however, depending on the problem they can sometimes describe unseen data rather poorly. On the other hand, a larger $\lambda$ in ridge does not necessarily lead to a sparse model, but rather, that the features tend to have a smaller magnitude. Ridge typically leads to a smoother function, which is desirable, since this avoids fitting of noise. However, Fransson *et al.* [127], found that other machine learning (ML) methods might be more suited for FCs fitting, such as automatic relevance determination regression (ARDR) or recursive feature elimination (RFE).

Linear support vector regression (SVR) is another type of regularization method, which, similarly to LASSO and Ridge penalizes large parameters. The difference lies in the objective function. The RMSE part of the object function has been replaced with a part that allows for small errors in the training data,

$$\min_{\mathbf{\Phi}} \left\{ \frac{1}{2} ||\mathbf{\Phi}||_2^2 + C \sum_i^l (\xi_i + \xi_i^*) \right\}.$$

C is a user defined constant which controls the trade-off between the norm of the features and how well the training data is described. $\xi_i$ and $\xi_i^*$ are slack parameters, which penalizes predictions that lie above or below a “tube“ of acceptable errors defined by the error margin, $\epsilon$. The problem can also be formulated in a slightly more explicit form,

$$\min_{\mathbf{\Phi}} \left\{ \frac{1}{2} ||\mathbf{\Phi}||_2^2 + C \sum_i^l \max\left(0, |y_i - A_{ji}\Phi_i| - \epsilon\right) \right\}.$$

Thus, the idea is similar to ridge, we want the features to be as small as possible, or rather, the function to be as smooth as possible. This is done by having some acceptable

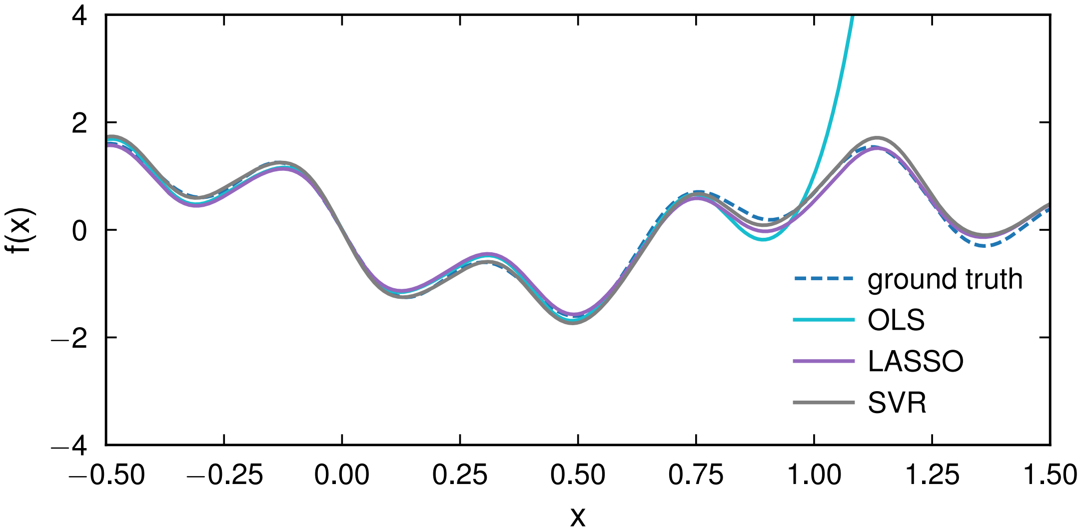

**Figure 7.1**: Comparing OLS, LASSO and SVR for a fictive regression problem

errors in the prediction, but too large errors gets penalized, for further information, see Ref. [128].

To demonstrate the strength of regularization, an arbitrary function is constructed as superposition of 4 sinusoidal waves. The amplitude acts as the parameter that we want to find and the wave act as the basis. To add some complexity, 3 more sinusoidal waves were included as basis functions. The function were sampled with 90 points that were randomly generated between 0 and 1 and a Gaussian noise, $\mathcal{N}(0, 0.6)$, was added. The resulting function and features are presented in Fig. 7.1 and Table 7.1. OLS represents the function very well inside the region where the samples have been drawn, however, it severely overestimates the function for x values larger than 1. We note that this is due to the severely over/underestimated coefficients. The regularized methods on the other hand describe the function significantly better, even outside the sampled region, with more reasonable features. Fortunately, this artificial problem is not a good representation of the FCs problem, where the OLS method actually performs decently,

| ground truth | 0.856 | 0 | 0.99 | 0.47 | 0.62 | 0 | 0 |
|---|---|---|---|---|---|---|---|
| OLS | 1329.44 | 2483.43 | -50.07 | 1384.53 | 0.66 | 0.06 | -1445.98 |
| LASSO | 0.00 | 0.00 | 0.62 | 0.00 | 0.63 | 0.04 | -0.52 |
| SVR | 0.08 | -0.22 | 0.79 | -0.06 | 0.65 | 0.04 | -0.39 |

**Table 7.1**: Amplitude of sinus wave with random frequency.

but it highlights the properties of the penalty term in the extreme cases.

### 7.1.3 Bayesian methods

Another set of regression methods is the Bayesian methods which utilizes Bayes theorem,

$$p(\boldsymbol{\Phi}|\mathrm{F}) = \frac{p(F|\boldsymbol{\Phi})p(\boldsymbol{\Phi})}{p(\mathbf{F})}, \tag{7.3}$$

where $p(\boldsymbol{\Phi}|F)$ is the posterior, $p(F|\boldsymbol{\Phi})$ the likelihood, $p(\boldsymbol{\Phi})$ are the prior and $p(\mathbf{F})$ the marginal likelihood. A typical algorithm from this formalism is, e.g., ARDR [129], where the prior over the features is constructed as a centered elliptical Gaussian. By imposing hyperpriors it is possible to find the covariance and standard deviation. ARDR allows for pruning of features with a slim distribution, i.e., features that most likely are irrelevant. The feature values that maximize the posterior is then taken as the solution. Conveniently, this formalism also allows us to draw parameters from the posterior to investigate the uncertainty of properties that are of interest, e.g., the phonon dispersion (see Chapter 6). The posterior can also be used to marginalize out the parameters and sample the uncertainty of new points.

An interesting note here is that some regularization algorithms can be understood from this formalism. For example, the ridge solution is the maximum posterior estimate of a Gaussian likelihood and a centered spherical Gaussian prior.

## 7.2 Correlation and Condition number

The likelihood in Equation (7.3) is commonly assumed to be a normal distribution (as in the case of ARDR),

$$\begin{aligned} p(\mathrm{F}|, \boldsymbol{\Phi}, \sigma) &= \frac{1}{(2\pi\sigma)^{N/2}} \exp\left(-\frac{1}{2\sigma^2}(\mathrm{A}\boldsymbol{\Phi} - \mathrm{F})^T(\mathrm{A}\boldsymbol{\Phi} - \mathrm{F})\right) \\ &\propto \exp\left(-\frac{1}{2\sigma^2}(\boldsymbol{\Phi} - \tilde{\boldsymbol{\Phi}})^T(\mathrm{A}^T\mathrm{A})(\boldsymbol{\Phi} - \tilde{\boldsymbol{\Phi}})\right). \end{aligned} \tag{7.4}$$

If we assume a uniform prior, $\boldsymbol{\Phi} \sim \mathcal{U}$, the posterior, which is a distribution of the features, $\boldsymbol{\Phi}$, will be identical to the likelihood. In that case, we can identify the mean and covariance matrix of the features as,

$$\begin{aligned} \boldsymbol{\Sigma} &= (\sigma^{-2}\mathrm{A}^T\mathrm{A})^{-1} \\ \tilde{\boldsymbol{\Phi}} &= \frac{1}{\sigma^2}\boldsymbol{\Sigma}\mathrm{A}^T\mathrm{F}. \end{aligned} \tag{7.5}$$

Where $\tilde{\boldsymbol{\Phi}}$ is the OLS solution given in Eq. (7.2) and $C = \mathbf{A}^T\mathbf{A}$ is the cross-correlation matrix. For the best possible solution, we want the inversion of the cross-correlation matrix to be as well posed as possible. This means that, the cross-correlation matrix should include as much information as possible for each feature. That is, the data should ideally be drawn as if it were independent data. The cross-correlation matrix for such data will have a very slim distribution for the off-diagonal elements, see, e.g., Ref. [130] for more details.

Another related method of estimating how well posed the regression problem in Eq. (6.6) is, is the condition number. The condition number is the ratio of the largest and smallest singular value of the design matrix. The singular values are calculated as the square root of the eigenvalues of the cross-correlation matrix. That is, the condition number tells you how large the difference between the smallest and largest scaling of a general vector is. For an ill-conditioned problem, the condition number would be large, i.e, the scaling between two general vectors is very different. A severely conditioned problem have two or more linearly dependent columns in the design matrix, which gives an infinite condition number.

To demonstrate an example of correlations and the condition number, three design matrices were constructed for BZO. Only harmonic interactions were considered, the cutoff was set to 8 Å and the total number of features were 102. The snapshots were generated from the rattle, phonon and MD methods. The standard deviation of the rattled structures were set to 0.05 Å, and the temperature for the phonon and MD structures were 300 K. The columns in the design matrix, A, has been standardized, i.e., the distribution of the training data for a single feature has a standard deviation of one. Fig. 7.2 then shows the correlations between three harmonic features, ideally, the distributions should be the shape of a circle. However, as the figure depicts, the features have more or less the shape of an ellipse, meaning that the features are, to some extent, correlated. Moreover, the condition number and the average, minimum and maximum value from the cross-correlation matrix are summarized in Table 7.2, which has been multiplied by $10^3$ and normalized as described in [130]. For this specific example, the correlations between the features in the rattle snapshots seems to be on average the lowest. However, no general trends or conclusions between the three ways of generating snapshots can be drawn from this minimal analysis, that is, this serves only as an example.

| | $C_{\text{min}}$ | $C_{\text{max}}$ | $C_{\text{mean}}$ | condition number |
|---|---|---|---|---|
| rattle | 0.0000 | 1.2545 | 0.0278 | 41.3469 |
| phonon | 0.0000 | 5.8271 | 0.0885 | 57.4894 |
| MD | 0.0000 | 1.3010 | 0.0361 | 69.0985 |

**Table** 7.2: Condition number, minimum, maximum, and average correlation for the harmonic features of BZO within a cutoff of 8 Å. The total number of features are 102.

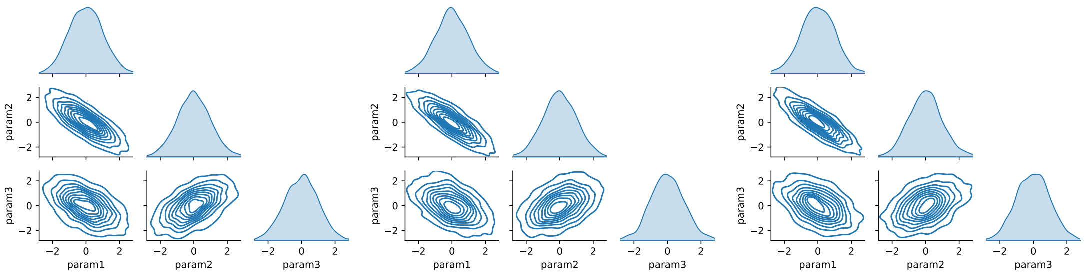

(a) (b) (c)

**Figure 7.2**: Visualization of correlations of the three most short ranged parameters in a training set from (a) rattle, (b) phonon and, (c) MD

### 7.2.1 Model performance

Finally, the performance of the model can be evaluated through cross validation, which measures how well the model is at predicting unseen data. Cross validation splits your data set into several different training and validation sets. The model is trained on the training set and tested on the validation set. This is repeated for all of the splits, and in the end you can check the performance of the model by, e.g., calculating an average score. The score is calculated via a loss function, a common loss function is the RMSE. The splits can be done in several different ways, but two has mainly been explored in this thesis, namely shuffle-split and KFold. KFold divides the data into $k$ sets, each set is then chosen once as a validation set, and the others are used as training examples. Shuffle-split randomizes $x$ number of validation sets in each iteration and the rest serves as training examples. The benefit of shuffle-split is that you can do as many splits as you'd like without making the training set smaller, which is a restriction of KFold. The benefit of KFold is that all data are used at least once as a validation set, which is not guaranteed in shuffle-split.

However, there are other loss functions that in addition to minimizing the error penalize the number of non-zero features in the model. One such loss function is the Bayesian information criterion (BIC),

$$\mathrm{BIC} = k \ln n - 2 \ln \hat{L}, \tag{7.6}$$

where k is the number of non-zero features, n is the number of samples and $\hat{L}$ is the maximized value of the likelihood function. BIC is calculated on the whole training set, i.e., there are no cross validation splits when evaluating a model using BIC. Commonly, both BIC and cross-validation are used in tandem to evaluate the performance of the model.

# 8

# Conclusion and Outlook

In **paper I**, the harmonic approximation was used to calculate the hydration enthalpy and entropy for BZO. We thoroughly investigate the vibrational spectrum of all atomic types and defect structures. From this, we deduced specific frequencies and modes that are of significant interest to the hydration thermodynamics. Direct comparison with experimental studies is difficult, as the van't Hoff plot shows a non-linear behavior, indicating two temperature regions with different hydration entropy and enthalpy. We find that the calculated hydration entropy agrees reasonably well with the reported experimental values in the high temperature range.

In **paper II**, the anharmonicity of the BZO structure has been explored, and more specifically, how it affects the frequency of the AFD mode. We constructed a fourth order FCP based on DFT data. The potential was then subsequently used to construct a SCPH model. In addition to the SCPH model, the potential was used to run MD. We showed that, it is pivotal to account for anharmonic interactions and quantum fluctuations to correctly capture the proper temperature dependence of the AFD mode in BZO.

Similar methods were applied in **Paper III** to study the very anharmonic perovskite $CsPbBr_3$. In this paper, the soft modes responsible for the continues-order phase transitions exhibited by $CsPbBr_3$ were explored. We found that these modes were overdamped significantly above the phase transition temperature.

A natural continuation of this work is to further investigate the hydration enthalpy and entropy for BZO, which is not completely understood. As mentioned above, the equilibrium constant shows a non-linear behavior experimentally, i.e., there exist a high and low temperature region. Therefore, there is undeniably something changing in the material around 500°C. Yamazaki *et al.* [49, 131] suggested that the deviation from linearity is due to a not negligible hole concentration at higher temperatures. This is something that was disputed by Kjølseth *et al.* [132], who argue that the non-linear behavior is more likely to be due to the clustering of yttrium dopants and oxygen vacancies at low temperatures. It has been shown that the oxygen vacancy gets strongly bound to the dopant [46], which leads to a less exothermic hydration enthalpy. The significant defect interactions will also very likely lead to a configurational disorder. This disorder should increase the configurational entropy of the defect cells, which could explain the significantly larger hydration entropy at lower temperatures. This could, for example, be investigated using CEs in further projects. Furthermore, it is also important to elaborate on the role of electron-holes in the hydration reaction of proton conducting membranes to further solidify the dynamics of the hydration reaction.

Although significant progress has been made in the manufacturing of well performing chemical reactors, electrolyzers and fuel cells [69, 133, 134], challenges remain. For example, electrolyzers suffer from slow electrode kinetics [134]. The role that proton association with defect traps plays for both the hydration reaction and the proton mobility is still elusive [12, 46, 132]. The effect of high concentrations of dopants on the sinterability and phase stability is also something that needs to be considered for further devices [135].

# Acknowledgments

Firstly, I would like to thank my supervisor, Göran Wahnström, for his eternal patience and invaluable support. Secondly, I would like to thank all the of the past and present members of the Condensed Matter and Materials Theory who has made this place an amazing workplace. I would also like to direct a special thanks to Hassan Ouhbi and Martin Gren, who has been amazing office mates. In addition to being an amazing office mate, Hassan helped me design the cover, which I am eternally grateful for. Further, I would also like to give a special thanks to Erik Fransson and Fredrik Eriksson, who has been invaluable in helping me with the force constant potentials and in general, phonon theory. Finally, I am grateful to all friends and family who never stopped believing in me. Especially my amazing partner, Amanda Lindenmeyer Asadi, who always stood by me even though I've been a train wreck during some periods.

# Bibliography

[1] J. D. Hunter, *Matplotlib: A 2D graphics environment,* Computing in Science & Engineering **9**, 90 (2007). `doi:10.1109/MCSE.2007.55`.

[2] A. Stukowski, *Visualization and analysis of atomistic simulation data with OVITO-the Open Visualization Tool,* MODELLING AND SIMULATION IN MATERIALS SCIENCE AND ENGINEERING **18**, (2010). `doi:{10.1088/0965-0393/18/1/015012}`.

[3] Inkscape Project, *Inkscape,* 2022. `https://inkscape.org`.

[4] G. Rose, *Mineralogisch-geognostische reise nach dem Ural, dem Altai un dem kaspischen meere* (Berlin, Verlag der Sanderschen buchandlung (C.W. Eichhoff), 1837).

[5] S. Jiang, T. Hu, J. Gild, N. Zhou, J. Nie, M. Qin, T. Harrington, K. Vecchio, and J. Luo, *A New Class of High-Entropy Perovskite Oxides,* Scripta Materialia **142**, 116 (2018). `doi:10.1016/j.scriptamat.2017.08.040`.

[6] C. M. Rost, E. Sachet, T. Borman, A. Moballegh, E. C. Dickey, D. Hou, J. L. Jones, S. Curtarolo, and J.-P. Maria, *Entropy-Stabilized Oxides,* Nature Communications **6**, 8485 (2015). `doi:10.1038/ncomms9485`.

[7] Y. Zhang, C.-K. Lim, Z. Dai, G. Yu, J. W. Haus, H. Zhang, and P. N. Prasad, *Photonics and Optoelectronics Using Nano-Structured Hybrid Perovskite Media and Their Optical Cavities,* Physics Reports **795**, 1 (2019). `doi:10.1016/j.physrep.2019.01.005`.

[8] A. Dey, J. Ye, A. De, E. Debroye, S. K. Ha, E. Bladt, A. S. Kshirsagar, Z. Wang, J. Yin, Y. Wang, L. N. Quan, F. Yan, M. Gao, X. Li, J. Shamsi, T. Debnath, M. Cao, M. A. Scheel, S. Kumar, J. A. Steele, M. Gerhard, L. Chouhan, K. Xu, X.-g. Wu, Y. Li, Y. Zhang, A. Dutta, C. Han, I. Vincon, A. L. Rogach, A. Nag, A. Samanta, B. A. Korgel, C.-J. Shih, D. R. Gamelin, D. H. Son, H. Zeng, H. Zhong, H. Sun, H. V. Demir, I. G. Scheblykin, I. Mora-Seró, J. K. Stolarczyk, J. Z. Zhang, J. Feldmann, J. Hofkens, J. M. Luther, J. Pérez-Prieto, L. Li, L. Manna, M. I. Bodnarchuk, M. V. Kovalenko, M. B. J. Roeffaers, N. Pradhan, O. F. Mohammed, O. M. Bakr, P. Yang, P. Müller-Buschbaum, P. V. Kamat, Q. Bao, Q. Zhang, R. Krahne, R. E. Galian, S. D. Stranks, S. Bals, V. Biju, W. A. Tisdale, Y. Yan, R. L. Z. Hoye, and L. Polavarapu, *State of the Art and Prospects for Halide Perovskite Nanocrystals,* ACS Nano **15**, 10775 (2021). `doi:10.1021/acsnano.0c08903`.

[9] W.-J. Yin, J.-H. Yang, J. Kang, Y. Yan, and S.-H. Wei, *Halide Perovskite Materials for Solar Cells: A Theoretical Review,* Journal of Materials Chemistry A **3**, 8926 (2015). `doi:10.1039/C4TA05033A`.

[10] A. K. Jena, A. Kulkarni, and T. Miyasaka, *Halide Perovskite Photovoltaics: Background, Status, and Future Prospects,* Chemical Reviews **119**, 3036 (2019). `doi:10.1021/acs.chemrev.8b00539`.

[11] N. Wang, H. Toriumi, Y. Sato, C. Tang, T. Nakamura, K. Amezawa, S. Kitano, H. Habazaki, and Y. Aoki, *$La_{0.8}Sr_{0.2}Co_{1-x}Ni_xO_{3-\delta}$ as the Efficient Triple Conductor Air Electrode for Protonic Ceramic Cells,* ACS Applied Energy Materials **4**, 554 (2021). `doi:10.1021/acsaem.0c02447`.

[12] Y. Yamazaki, F. Blanc, Y. Okuyama, L. Buannic, J. C. Lucio-Vega, C. P. Grey, and S. M. Haile, *Proton Trapping in Yttrium-Doped Barium Zirconate,* Nature Materials **12**, 647 (2013). `doi:10.1038/nmat3638`.

[13] M.-H. Zhang, K. Wang, Y.-J. Du, G. Dai, W. Sun, G. Li, D. Hu, H. C. Thong, C. Zhao, X.-Q. Xi, Z.-X. Yue, and J.-F. Li, *High and Temperature-Insensitive Piezoelectric Strain in Alkali Niobate Lead-free Perovskite,* Journal of the American Chemical Society **139**, 3889 (2017). `doi:10.1021/jacs.7b00520`.

[14] I. H. Lone, J. Aslam, N. R. E. Radwan, A. H. Bashal, A. F. A. Ajlouni, and A. Akhter, *Multiferroic $ABO_3$ Transition Metal Oxides: A Rare Interaction of Ferroelectricity and Magnetism,* Nanoscale Research Letters **14**, 142 (2019). `doi:10.1186/s11671-019-2961-7`.

[15] H. Tamura, T. Konoike, Y. Sakabe, and K. Wakino, *Improved High-Q Dielectric Resonator with Complex Perovskite Structure,* Journal of the American Ceramic Society **67**, c59 (1984). `doi:10.1111/j.1151-2916.1984.tb18828.x`.

[16] W. Zhong, C.-T. Au, and Y.-W. Du, *Review of Magnetocaloric Effect in Perovskite-Type Oxides,* Chinese Physics B **22**, 057501 (2013). `doi:10.1088/1674-1056/22/5/057501`.

[17] V. M. Goldschmidt, *Die Gesetze der Krystallochemie,* Naturwissenschaften **14**, 477 (1926). `doi:10.1007/BF01507527`.

[18] R. D. Shannon, *Revised Effective Ionic Radii and Systematic Studies of Interatomic Distances in Halides and Chalcogenides,* Acta Crystallographica Section A **32**, 751 (1976). `doi:10.1107/S0567739476001551`.

[19] K. M. Rabe, C. H. Ahn, and J.-M. Triscone, eds., *Physics of Ferroelectrics: A Modern Perspective* (Berlin ; New York: Springer, 2007). ISBN 978-3-540-34590-9.

[20] S. Sasaki, C. T. Prewitt, J. D. Bass, and W. A. Schulze, *Orthorhombic Perovskite $CaTiO_3$ and $CdTiO_3$: Structure and Space Group,* Acta Crystallographica Section C Crystal Structure Communications **43**, 1668 (1987). `doi:10.1107/S0108270187090620`.

[21] M. Swift, A. Janotti, and C. G. Van de Walle, *Small Polarons and Point Defects in Barium Cerate,* Physical Review B **92**, 214114 (2015). `doi:10.1103/PhysRevB.92.214114`.

[22] W. Zhong and D. Vanderbilt, *Competing Structural Instabilities in Cubic Perovskites,* Physical Review Letters **74**, 2587 (1995). `doi:10.1103/PhysRevLett.74.2587`.

[23] A. R. Akbarzadeh, I. Kornev, C. Malibert, L. Bellaiche, and J. M. Kiat, *Combined Theoretical and Experimental Study of the Low-Temperature Properties of $BaZrO_3$,* Physical Review B **72**, 205104 (2005). `doi:10.1103/PhysRevB.72.205104`.

[24] F. Giannici, M. Shirpour, A. Longo, A. Martorana, R. Merkle, and J. Maier, *Long-Range and Short-Range Structure of Proton-Conducting Y:$BaZrO_3$,* Chemistry of Materials **23**, 2994 (2011). `doi:10.1021/cm200682d`.

[25] I. Levin, M. G. Han, H. Y. Playford, V. Krayzman, Y. Zhu, and R. A. Maier, *Nanoscale-Correlated Octahedral Rotations in BaZrO$_3$,* Physical Review B **104**, 214109 (2021). `doi:10.1103/PhysRevB.104.214109`.

[26] A. Perrichon, E. Jedvik Granhed, G. Romanelli, A. Piovano, A. Lindman, P. Hyldgaard, G. Wahnström, and M. Karlsson, *Unraveling the Ground-State Structure of BaZrO$_3$ by Neutron Scattering Experiments and First-Principles Calculations,* Chemistry of Materials **32**, 2824 (2020). `doi:10.1021/acs.chemmater.9b04437`.

[27] R. A. Evarestov, *Hybrid Density Functional Theory LCAO Calculations on Phonons in Ba(Ti,Zr,Hf)O$_3$,* Physical Review B **83**, 014105 (2011). `doi:10.1103/PhysRevB.83.014105`.

[28] T. S. Bjørheim, E. A. Kotomin, and J. Maier, *Hydration Entropy of BaZrO$_3$ from First Principles Phonon Calculations,* Journal of Materials Chemistry A **3**, 7639 (2015). `doi:10.1039/C4TA06880G`.

[29] A. I. Lebedev and I. A. Sluchinskaya, *Structural Instability in BaZrO$_3$ Crystals: Calculations and Experiment,* Physics of the Solid State **55**, 1941 (2013). `doi:10.1134/S1063783413090229`.

[30] A. Bilić and J. D. Gale, *Ground State Structure of BaZrO$_3$ : A Comparative First-Principles Study,* Physical Review B **79**, 174107 (2009). `doi:10.1103/PhysRevB.79.174107`.

[31] C. Toulouse, D. Amoroso, C. Xin, P. Veber, M. C. Hatnean, G. Balakrishnan, M. Maglione, P. Ghosez, J. Kreisel, and M. Guennou, *Lattice Dynamics and Raman Spectrum of BaZrO$_3$ Single Crystals,* Physical Review B **100**, 134102 (2019). `doi:10.1103/PhysRevB.100.134102`.

[32] B. Guillaume, F. Boschini, I. Garcia-Cano, A. Rulmont, R. Cloots, and M. Ausloos, *Optimization of BaZrO$_3$ Sintering by Control of the Initial Powder Size Distribution; a Factorial Design Statistical Analysis,* Journal of the European Ceramic Society **25**, 3593 (2005). `doi:10.1016/j.jeurceramsoc.2004.09.022`.

[33] I. Charrier-Cougoulic, T. Pagnier, and G. Lucazeau, *Raman Spectroscopy of Perovskite-Type BaCe$_x$Zr$_{1-x}$O$_3$(0≤x≤1),* Journal of Solid State Chemistry **142**, 220 (1999). `doi:10.1006/jssc.1998.8038`.

[34] S. Mori, *Phase Transformation in Barium Orthoferrate, BaFeO$_{3-x}$,* Journal of the American Ceramic Society **49**, 600 (1966). `doi:10.1111/j.1151-2916.1966.tb13176.x`.

[35] S. Mori, *Preparation of Various Phases of BaFeO$_{3-x}$,* Journal of the American Ceramic Society **48**, 165 (1965). `doi:10.1111/j.1151-2916.1965.tb16058.x`.

[36] N. Hayashi, T. Yamamoto, H. Kageyama, M. Nishi, Y. Watanabe, T. Kawakami, Y. Matsushita, A. Fujimori, and M. Takano, *BaFeO$_3$: A Ferromagnetic Iron Oxide,* Angewandte Chemie International Edition **50**, 12547 (2011). `doi:10.1002/anie.201105276`.

[37] X. Zhu, H. Wang, and W. Yang, *Structural Stability and Oxygen Permeability of Cerium Lightly Doped BaFeO$_{3-\delta}$ Ceramic Membranes,* Solid State Ionics **177**, 2917 (2006). `doi:10.1016/j.ssi.2006.08.027`.

[38] C. Callender, D. P. Norton, R. Das, A. F. Hebard, and J. D. Budai, *Ferromagnetism in Pseudocubic BaFeO$_3$ Epitaxial Films,* Applied Physics Letters **92**, 012514 (2008). `doi:10.1063/1.2832768`.

[39] T. Matsui, H. Tanaka, N. Fujimura, T. Ito, H. Mabuchi, and K. Morii, *Structural, Dielectric, and Magnetic Properties of Epitaxially Grown* $BaFeO_3$ *Thin Films on (100)* $SrTiO_3$ *Single-Crystal Substrates,* Applied Physics Letters **81**, 2764 (2002). `doi:10.1063/1.1513213`.

[40] G. Rahman, J. M. Morbec, R. Ferradás, V. M. García-Suárez, and N. J. English, *Distortion Induced Magnetic Phase Transition in Cubic* $BaFeO_3$*,* Journal of Magnetism and Magnetic Materials **401**, 1097 (2016). `doi:10.1016/j.jmmm.2015.11.002`.

[41] I. Cherair, E. Bousquet, M. Schmitt, N. Iles, and A. Kellou, *Strain Induced Jahn-Teller Distortions in* $BaFeO_3$ *: A First-Principles Study,* Journal of Physics: Condensed Matter **30**, (2017). `doi:10.1088/1361-648X/aac46d`.

[42] M. F. Hoedl, D. Gryaznov, R. Merkle, E. A. Kotomin, and J. Maier, *Interdependence of Oxygenation and Hydration in Mixed-Conducting* $(Ba,Sr)FeO_{3-\delta}$ *Perovskites Studied by Density Functional Theory,* The Journal of Physical Chemistry C **124**, 11780 (2020). `doi:10.1021/acs.jpcc.0c01924`.

[43] H. A. Jahn, E. Teller, and F. G. Donnan, *Stability of Polyatomic Molecules in Degenerate Electronic States - I—Orbital Degeneracy,* Proceedings of the Royal Society of London. Series A - Mathematical and Physical Sciences **161**, 220 (1937). `doi:10.1098/rspa.1937.0142`.

[44] J. Conradie, *Jahn-Teller Effect in High Spin* $D^4$ *and* $D^9$ *Octahedral Metal-Complexes,* Inorganica Chimica Acta **486**, 193 (2019). `doi:10.1016/j.ica.2018.10.040`.

[45] M. D. McCluskey and A. Janotti, *Defects in Semiconductors,* Journal of Applied Physics **127**, 190401 (2020). `doi:10.1063/5.0012677`.

[46] M. E. Björketun, P. G. Sundell, and G. Wahnström, *Structure and Thermodynamic Stability of Hydrogen Interstitials in* $BaZrO_3$ *Perovskite Oxide from Density Functional Calculations,* Faraday Discussions **134**, 247 (2006). `doi:10.1039/B602081J`.

[47] K. Kreuer, *Proton-Conducting Oxides,* Annual Review of Materials Research **33**, 333 (2003). `doi:10.1146/annurev.matsci.33.022802.091825`.

[48] K. D. Kreuer, S. Adams, W. Münch, A. Fuchs, U. Klock, and J. Maier, *Proton Conducting Alkaline Earth Zirconates and Titanates for High Drain Electrochemical Applications,* Solid State Ionics **145**, 295 (2001). `doi:10.1016/S0167-2738(01)00953-5`.

[49] Y. Yamazaki, P. Babilo, and S. M. Haile, *Defect Chemistry of Yttrium-Doped Barium Zirconate: A Thermodynamic Analysis of Water Uptake,* Chemistry of Materials **20**, 6352 (2008). `doi:10.1021/cm800843s`.

[50] K. Toyoura, W. Meng, D. Han, and T. Uda, *Preferential Proton Conduction along a Three-Dimensional Dopant Network in Yttrium-Doped Barium Zirconate: A First-Principles Study,* Journal of Materials Chemistry A **6**, 22721 (2018). `doi:10.1039/C8TA08283A`.

[51] L. P. Putilov and V. I. Tsidilkovski, *Impact of Bound Ionic Defects on the Hydration of Acceptor-Doped Proton-Conducting Perovskites,* Physical Chemistry Chemical Physics **21**, 6391 (2019). `doi:10.1039/C8CP07745B`.

[52] A. Løken, S. W. Saeed, M. N. Getz, X. Liu, and T. S. Bjørheim, *Alkali Metals as Efficient A-site Acceptor Dopants in Proton Conducting* $BaZrO_3$*,* Journal of Materials Chemistry A **4**, 9229 (2016). `doi:10.1039/C6TA01446A`.

[53] J. L. Ramsey, *On Not Defining Sustainability,* Journal of Agricultural and Environmental Ethics **28**, 1075 (2015). `doi:10.1007/s10806-015-9578-3`.

[54] *1987: Brundtland Report,* https://www.are.admin.ch/are/en/home/nachhaltige-entwicklung/internationale-zusammenarbeit/agenda-2030-fuer-nachhaltige-entwicklung/uno-_-meilensteine-zur-nachhaltigen-entwicklung/1987–brundtland-bericht.html.

[55] N. Armaroli and V. Balzani, *The Legacy of Fossil Fuels,* Chemistry – An Asian Journal **6**, 768 (2011). `doi:10.1002/asia.201000797`.

[56] F. P. Perera, *Multiple Threats to Child Health from Fossil Fuel Combustion: Impacts of Air Pollution and Climate Change,* Environmental Health Perspectives **125**, 141 (2017). `doi:10.1289/EHP299`.

[57] A. Sommer, *Burning Fossil Fuels: Impact of Climate Change on Health,* International Journal of Health Services **46**, 48 (2016). `doi:10.1177/0020731415625253`.

[58] W. Kreuter and H. Hofmann, *Electrolysis: The Important Energy Transformer in a World of Sustainable Energy,* International Journal of Hydrogen Energy **23**, 661 (1998). `doi:10.1016/S0360-3199(97)00109-2`.

[59] G. W. Crabtree, M. S. Dresselhaus, and M. V. Buchanan, *The Hydrogen Economy,* Physics Today **57**, 39 (2004). `doi:10.1063/1.1878333`.

[60] S. C. Singhal, *Solid Oxide Fuel Cells for Stationary, Mobile, and Military Applications,* Solid State Ionics **152–153**, 405 (2002). `doi:10.1016/S0167-2738(02)00349-1`.

[61] R. Mark Ormerod, *Solid Oxide Fuel Cells,* Chemical Society Reviews **32**, 17 (2003). `doi:10.1039/B105764M`.

[62] E. Fabbri, L. Bi, D. Pergolesi, and E. Traversa, *Towards the Next Generation of Solid Oxide Fuel Cells Operating Below 600 °C with Chemically Stable Proton-Conducting Electrolytes,* Advanced Materials **24**, 195 (2012). `doi:10.1002/adma.201103102`.

[63] E. D. Wachsman and K. T. Lee, *Lowering the Temperature of Solid Oxide Fuel Cells,* Science **334**, 935 (2011). `doi:10.1126/science.1204090`.

[64] K. Amezawa, K. Mizuno, S. Kageyama, K. Nishidate, T. Imaizumi, Y. Kimura, T. Nakamura, K. Yashiro, F. Iguchi, and T. Kawada, *(Invited) Contribution of Triple/Double Phase Boundary Reactions in Mixed Conducting Oxide Cathodes in SOFCs and PCFCs,* ECS Meeting Abstracts **MA2020-02**, 2526 (2020). `doi:10.1149/MA2020-02402526mtgabs`.

[65] J. Wang, Z. Li, H. Zang, Y. Sun, Y. Zhao, Z. Wang, Z. Zhu, Z. Wei, and Q. Zheng, $BaZr_{0.1}Fe_{0.9-x}NixO_{3-\delta}$ *Cubic Perovskite Oxides for Protonic Ceramic Fuel Cell Cathodes,* International Journal of Hydrogen Energy **47**, 9395 (2022). `doi:10.1016/j.ijhydene.2022.01.012`.

[66] S. Wang, J. Shen, Z. Zhu, Z. Wang, Y. Cao, X. Guan, Y. Wang, Z. Wei, and M. Chen, *Further Optimization of Barium Cerate Properties via Co-Doping Strategy for Potential Application as Proton-Conducting Solid Oxide Fuel Cell Electrolyte,* Journal of Power Sources **387**, 24 (2018). `doi:10.1016/j.jpowsour.2018.03.054`.

[67] J. Tong, D. Clark, L. Bernau, A. Subramaniyan, and R. O'Hayre, *Proton-Conducting Yttrium-Doped Barium Cerate Ceramics Synthesized by a Cost-Effective Solid-State Reactive Sintering Method,* Solid State Ionics **181**, 1486 (2010). `doi:10.1016/j.ssi.2010.08.022`.

[68] J. Tong, D. Clark, M. Hoban, and R. O'Hayre, *Cost-Effective Solid-State Reactive Sintering Method for High Conductivity Proton Conducting Yttrium-Doped Barium Zirconium Ceramics,* Solid State Ionics **181**, 496 (2010). `doi:10.1016/j.ssi.2010.02.008`.

[69] C. Duan, R. J. Kee, H. Zhu, C. Karakaya, Y. Chen, S. Ricote, A. Jarry, E. J. Crumlin, D. Hook, R. Braun, N. P. Sullivan, and R. O'Hayre, *Highly Durable, Coking and Sulfur Tolerant, Fuel-Flexible Protonic Ceramic Fuel Cells,* Nature **557**, 217 (2018). `doi:10.1038/s41586-018-0082-6`.

[70] C. Duan, R. Kee, H. Zhu, N. Sullivan, L. Zhu, L. Bian, D. Jennings, and R. O'Hayre, *Highly Efficient Reversible Protonic Ceramic Electrochemical Cells for Power Generation and Fuel Production,* Nature Energy **4**, 230 (2019). `doi:10.1038/s41560-019-0333-2`.

[71] M. Born and R. Oppenheimer, *Zur Quantentheorie Der Molekeln,* Annalen der Physik **389**, 457 (1927). `doi:10.1002/andp.19273892002`.

[72] P. L. Taylor and O. Heinonen, *A Quantum Approach to Condensed Matter Physics* (Cambridge: Cambridge University Press, 2002). ISBN 978-0-521-77103-0. `doi:10.1017/CBO9780511998782`.

[73] P. Hohenberg and W. Kohn, *Inhomogeneous Electron Gas,* Physical Review **136**, B864 (1964). `doi:10.1103/PhysRev.136.B864`.

[74] L. H. Thomas, *The Calculation of Atomic Fields,* Mathematical Proceedings of the Cambridge Philosophical Society **23**, 542 (1927). `doi:10.1017/S0305004100011683`.

[75] Fermi, Enrico, *Un Metodo Statistico per La Determinazione Di Alcune Priorieta Dell'atome,* Rend. Accad. Naz. Lincei **6**, 602 (1927).

[76] P. A. M. Dirac, *Note on Exchange Phenomena in the Thomas Atom,* Mathematical Proceedings of the Cambridge Philosophical Society **26**, 376 (1930). `doi:10.1017/S0305004100016108`.

[77] W. Kohn and L. J. Sham, *Self-Consistent Equations Including Exchange and Correlation Effects,* Physical Review **140**, A1133 (1965). `doi:10.1103/PhysRev.140.A1133`.

[78] A. D. Becke, *Perspective: Fifty Years of Density-Functional Theory in Chemical Physics,* The Journal of Chemical Physics **140**, 18A301 (2014). `doi:10.1063/1.4869598`.

[79] R. O. Jones, *Density Functional Theory: Its Origins, Rise to Prominence, and Future,* Reviews of Modern Physics **87**, 897 (2015). `doi:10.1103/RevModPhys.87.897`.

[80] W. Kohn, *Nobel Lecture: Electronic Structure of Matter—Wave Functions and Density Functionals,* Reviews of Modern Physics **71**, 1253 (1999). `doi:10.1103/RevModPhys.71.1253`.

[81] R. M. Martin, *Electronic Structure: Basic Theory and Practical Methods* (Cambridge University Press, 2020). ISBN 978-1-108-65747-1.

[82] E. Wigner, *Effects of the Electron Interaction on the Energy Levels of Electrons in Metals,* Transactions of the Faraday Society **34**, 678 (1938). `doi:10.1039/TF9383400678`.

[83] E. Wigner, *On the Interaction of Electrons in Metals,* Physical Review **46**, 1002 (1934). `doi:10.1103/PhysRev.46.1002`.

[84] M. Gell-Mann and K. A. Brueckner, *Correlation Energy of an Electron Gas at High Density,* Physical Review **106**, 364 (1957). `doi:10.1103/PhysRev.106.364`.

[85] D. M. Ceperley and B. J. Alder, *Ground State of the Electron Gas by a Stochastic Method,* Physical Review Letters **45**, 566 (1980). `doi:10.1103/PhysRevLett.45.566`.

[86] J. P. Perdew, K. Burke, and M. Ernzerhof, *Generalized Gradient Approximation Made Simple,* Physical Review Letters **77**, 3865 (1996). `doi:10.1103/PhysRevLett.77.3865`.

[87] M. G. Medvedev, I. S. Bushmarinov, J. Sun, J. P. Perdew, and K. A. Lyssenko, *Density Functional Theory Is Straying from the Path toward the Exact Functional,* Science **355**, 49 (2017). `doi:10.1126/science.aah5975`.

[88] J. P. Perdew and A. Zunger, *Self-Interaction Correction to Density-Functional Approximations for Many-Electron Systems,* Physical Review B **23**, 5048 (1981). `doi:10.1103/PhysRevB.23.5048`.

[89] J. P. Perdew and M. Levy, *Physical Content of the Exact Kohn-Sham Orbital Energies: Band Gaps and Derivative Discontinuities,* Physical Review Letters **51**, 1884 (1983). `doi:10.1103/PhysRevLett.51.1884`.

[90] P. Mori-Sánchez, A. J. Cohen, and W. Yang, *Localization and Delocalization Errors in Density Functional Theory and Implications for Band-Gap Prediction,* Physical Review Letters **100**, 146401 (2008). `doi:10.1103/PhysRevLett.100.146401`.

[91] S. L. Dudarev, G. A. Botton, S. Y. Savrasov, C. J. Humphreys, and A. P. Sutton, *Electron-Energy-Loss Spectra and the Structural Stability of Nickel Oxide: An LSDA+U Study,* Physical Review B **57**, 1505 (1998). `doi:10.1103/PhysRevB.57.1505`.

[92] H. J. Kulik, *Perspective: Treating Electron over-Delocalization with the DFT+U Method,* The Journal of Chemical Physics **142**, 240901 (2015). `doi:10.1063/1.4922693`.

[93] E. J. Granhed, A. Lindman, C. Eklöf-Österberg, M. Karlsson, S. F. Parker, and G. Wahnström, *Band vs. Polaron: Vibrational Motion and Chemical Expansion of Hydride Ions as Signatures for the Electronic Character in Oxyhydride Barium Titanate,* Journal of Materials Chemistry A **7**, 16211 (2019). `doi:10.1039/C9TA00086K`.

[94] J. P. Perdew, M. Ernzerhof, and K. Burke, *Rationale for Mixing Exact Exchange with Density Functional Approximations,* The Journal of Chemical Physics **105**, 9982 (1996). `doi:10.1063/1.472933`.

[95] J. Paier, R. Hirschl, M. Marsman, and G. Kresse, *The Perdew–Burke–Ernzerhof Exchange-Correlation Functional Applied to the G2-1 Test Set Using a Plane-Wave Basis Set,* The Journal of Chemical Physics **122**, 234102 (2005). `doi:10.1063/1.1926272`.

[96] A. V. Krukau, O. A. Vydrov, A. F. Izmaylov, and G. E. Scuseria, *Influence of the Exchange Screening Parameter on the Performance of Screened Hybrid Functionals,* The Journal of Chemical Physics **125**, 224106 (2006). `doi:10.1063/1.2404663`.

[97] W. E. Pickett, *Pseudopotential Methods in Condensed Matter Applications,* Computer Physics Reports **9**, 115 (1989). `doi:10.1016/0167-7977(89)90002-6`.

[98] D. R. Hamann, M. Schlüter, and C. Chiang, *Norm-Conserving Pseudopotentials,* Physical Review Letters **43**, 1494 (1979). `doi:10.1103/PhysRevLett.43.1494`.

[99] D. Vanderbilt, *Soft Self-Consistent Pseudopotentials in a Generalized Eigenvalue Formalism,* Physical Review B **41**, 7892 (1990). `doi:10.1103/PhysRevB.41.7892`.

[100] P. E. Blöchl, *Projector Augmented-Wave Method,* Physical Review B **50**, 17953 (1994). `doi:10.1103/PhysRevB.50.17953`.

[101] A. Togo and I. Tanaka, *First Principles Phonon Calculations in Materials Science,* Scripta Materialia **108**, 1 (2015). `doi:10.1016/j.scriptamat.2015.07.021`.

[102] F. Eriksson, E. Fransson, and P. Erhart, *The Hiphive Package for the Extraction of High-Order Force Constants by Machine Learning,* Advanced Theory and Simulations **2**, 1800184 (2019). `doi:10.1002/adts.201800184`.

[103] K. Parlinski, Z. Q. Li, and Y. Kawazoe, *First-Principles Determination of the Soft Mode in Cubic* $ZrO_2$*,* Physical Review Letters **78**, 4063 (1997). `doi:10.1103/PhysRevLett.78.4063`.

[104] X. Gonze, J.-C. Charlier, D. Allan, and M. Teter, *Interatomic Force Constants from First Principles: The Case of $\alpha$-Quartz,* Physical Review B **50**, 13035 (1994). `doi:10.1103/PhysRevB.50.13035`.

[105] B. Fultz, *Vibrational Thermodynamics of Materials,* Progress in Materials Science **55**, 247 (2010). `doi:10.1016/j.pmatsci.2009.05.002`.

[106] S. Rossano, F. Mauri, C. J. Pickard, and I. Farnan, *First-Principles Calculation of $^{17}O$ and $^{25}Mg$ NMR Shieldings in MgO at Finite Temperature: Rovibrational Effect in Solids,* The Journal of Physical Chemistry B **109**, 7245 (2005). `doi:10.1021/jp044251w`.

[107] I. Errea, M. Calandra, and F. Mauri, *Anharmonic Free Energies and Phonon Dispersions from the Stochastic Self-Consistent Harmonic Approximation: Application to Platinum and Palladium Hydrides,* Physical Review B **89**, 064302 (2014). `doi:10.1103/PhysRevB.89.064302`.

[108] A. Togo, L. Chaput, and I. Tanaka, *Distributions of Phonon Lifetimes in Brillouin Zones,* Physical Review B **91**, 094306 (2015). `doi:10.1103/PhysRevB.91.094306`.

[109] O. Hellman and I. A. Abrikosov, *Temperature-Dependent Effective Third-Order Interatomic Force Constants from First Principles,* Physical Review B **88**, 144301 (2013). `doi:10.1103/PhysRevB.88.144301`.

[110] A. A. Maradudin and A. E. Fein, *Scattering of Neutrons by an Anharmonic Crystal,* Physical Review **128**, 2589 (1962). `doi:10.1103/PhysRev.128.2589`.

[111] A. van Roekeghem, J. Carrete, and N. Mingo, *Anomalous Thermal Conductivity and Suppression of Negative Thermal Expansion in* $ScF_3$*,* Physical Review B , 5 (2016).

[112] Q. Zhang, J. Ding, and M. He, *First Principles Study on Structural, Lattice Dynamical and Thermal Properties of* $BaCeO_3$*,* Journal of Physics and Chemistry of Solids **108**, 76 (2017). `doi:10.1016/j.jpcs.2017.04.019`.

[113] P. Souvatzis, O. Eriksson, M. I. Katsnelson, and S. P. Rudin, *The Self-Consistent Ab Initio Lattice Dynamical Method,* Computational Materials Science **44**, 888 (2009). `doi:10.1016/j.commatsci.2008.06.016`.

[114] O. Hellman, I. A. Abrikosov, and S. I. Simak, *Lattice Dynamics of Anharmonic Solids from First Principles,* Physical Review B **84**, 180301 (2011). `doi:10.1103/PhysRevB.84.180301`.

[115] L. T. Kong, *Phonon Dispersion Measured Directly from Molecular Dynamics Simulations,* Computer Physics Communications **182**, 2201 (2011). `doi:10.1016/j.cpc.2011.04.019`.

[116] T. Tadano and S. Tsuneyuki, *Self-Consistent Phonon Calculations of Lattice Dynamical Properties in Cubic* $SrTiO_3$ *with First-Principles Anharmonic Force Constants,* Physical Review B **92**, 054301 (2015). `doi:10.1103/PhysRevB.92.054301`.

[117] O. Hellman, P. Steneteg, I. A. Abrikosov, and S. I. Simak, *Temperature Dependent Effective Potential Method for Accurate Free Energy Calculations of Solids,* Physical Review B **87**, 104111 (2013). `doi:10.1103/PhysRevB.87.104111`.

[118] E. Metsanurk and M. Klintenberg, *Sampling-Dependent Systematic Errors in Effective Harmonic Models,* Physical Review B **99**, 184304 (2019). `doi:10.1103/PhysRevB.99.184304`.

[119] J. Behler and M. Parrinello, *Generalized Neural-Network Representation of High-Dimensional Potential-Energy Surfaces,* Physical Review Letters **98**, 146401 (2007). `doi:10.1103/PhysRevLett.98.146401`.

[120] R. Jinnouchi, K. Miwa, F. Karsai, G. Kresse, and R. Asahi, *On-the-Fly Active Learning of Interatomic Potentials for Large-Scale Atomistic Simulations,* The Journal of Physical Chemistry Letters **11**, 6946 (2020). `doi:10.1021/acs.jpclett.0c01061`.

[121] A. P. Bartók, R. Kondor, and G. Csányi, *On Representing Chemical Environments,* Physical Review B **87**, 184115 (2013). `doi:10.1103/PhysRevB.87.184115`.

[122] A. Stukowski, E. Fransson, M. Mock, and P. Erhart, *Atomicrex—a General Purpose Tool for the Construction of Atomic Interaction Models,* Modelling and Simulation in Materials Science and Engineering **25**, 055003 (2017). `doi:10.1088/1361-651X/aa6ecf`.

[123] E. Fransson, M. Slabanja, P. Erhart, and G. Wahnström, *Dynasor—A Tool for Extracting Dynamical Structure Factors and Current Correlation Functions from Molecular Dynamics Simulations,* Advanced Theory and Simulations **4**, 2000240 (2021). `doi:10.1002/adts.202000240`.

[124] J. Cao and G. A. Voth, *The Formulation of Quantum Statistical Mechanics Based on the Feynman Path Centroid Density. I. Equilibrium Properties,* The Journal of Chemical Physics **100**, 5093 (1994). `doi:10.1063/1.467175`.

[125] M. H. Müser, *Simulation of Material Properties below the Debye Temperature: A Path-Integral Molecular Dynamics Case Study of Quartz,* The Journal of Chemical Physics **114**, 6364 (2001). `doi:10.1063/1.1355772`.

[126] G. Grosso and G. P. Parravicini, *Chapter 10 - Scattering of Particles by Crystals,* in *Solid State Physics (Second Edition)*, edited by G. Grosso and G. P. Parravicini (Amsterdam: Academic Press, 2014), p. 437. `doi:10.1016/B978-0-12-385030-0.00010-4`.

[127] E. Fransson, F. Eriksson, and P. Erhart, *Efficient Construction of Linear Models in Materials Modeling and Applications to Force Constant Expansions,* npj Computational Materials **6**, 1 (2020). `doi:10.1038/s41524-020-00404-5`.

[128] A. J. Smola and B. Schölkopf, *A Tutorial on Support Vector Regression,* Statistics and Computing **14**, 199 (2004). `doi:10.1023/B:STCO.0000035301.49549.88`.

[129] M. E. Tipping, *Sparse Bayesian Learning and the Relevance Vector Machine,* The Journal of Machine Learning Research **1**, 211 (2001). `doi:10.1162/15324430152748236`.

[130] L. J. Nelson, V. Ozolinsˇ, C. S. Reese, F. Zhou, and G. L. W. Hart, *Cluster Expansion Made Easy with Bayesian Compressive Sensing,* Physical Review B , 10 (2013).

[131] Y. Yamazaki, C.-K. Yang, and S. M. Haile, *Unraveling the Defect Chemistry and Proton Uptake of Yttrium-Doped Barium Zirconate,* Scripta Materialia **65**, 102 (2011). `doi:10.1016/j.scriptamat.2010.12.034`.

[132] C. Kjølseth, L.-Y. Wang, R. Haugsrud, and T. Norby, *Determination of the Enthalpy of Hydration of Oxygen Vacancies in Y-doped* $BaZrO_3$ *and* $BaCeO_3$ *by TG-DSC,* Solid State Ionics **181**, 1740 (2010). `doi:10.1016/j.ssi.2010.10.005`.

[133] D. Clark, H. Malerød-Fjeld, M. Budd, I. Yuste-Tirados, D. Beeaff, S. Aamodt, K. Nguyen, L. Ansaloni, T. Peters, P. K. Vestre, D. K. Pappas, M. I. Valls, S. Remiro-Buenamañana, T. Norby, T. S. Bjørheim, J. M. Serra, and C. Kjølseth, *Single-Step Hydrogen Production from NH3, CH4, and Biogas in Stacked Proton Ceramic Reactors,* Science **376**, 390 (2022). `doi:10.1126/science.abj3951`.

[134] E. Vøllestad, R. Strandbakke, M. Tarach, D. Catalán-Martínez, M.-L. Fontaine, D. Beeaff, D. R. Clark, J. M. Serra, and T. Norby, *Mixed Proton and Electron Conducting Double Perovskite Anodes for Stable and Efficient Tubular Proton Ceramic Electrolysers,* Nature Materials **18**, 752 (2019). `doi:10.1038/s41563-019-0388-2`.

[135] C. Y. R. Vera, H. Ding, D. Peterson, W. T. Gibbons, M. Zhou, and D. Ding, *A Mini-Review on Proton Conduction of BaZrO3-based Perovskite Electrolytes,* Journal of Physics: Energy **3**, 032019 (2021). `doi:10.1088/2515-7655/ac12ab`.